Angewandte Chemie
Eine Zeitschrift der Gesellschaft Deutscher Chemiker

Supporting Information

An Adaptable N-Heterocyclic Carbene Macrocycle Hosting Copper in Three Oxidation States

*Yang Liu, Stefan G. Resch, Iris Klawitter, George E. Cutsail III, Serhiy Demeshko, Sebastian Dechert, Fritz E. Kühn, Serena DeBeer, and Franc Meyer**

anie_201912745_sm_miscellaneous_information.pdf

Table of Contents

Experimental Procedures

General Considerations. All manipulations on air- and moisture-sensitive materials were performed under an atmosphere of dry dinitrogen with the rigid exclusion of air and moisture using standard Schlenk or cannula techniques, or in a glovebox. Solvents were dried with sodium (Et_2O, THF and Hexane) in the presence of benzophenone or CaH_2 (MeCN) and freshly distilled and degassed prior use. [D_3]MeCN was dried with 3 Å molecular sieves. [D_6]Acetone was dried with dry K_2CO_3, and freshly distilled and degassed prior use. [H_2L](PF_6)$_2$,[1] [MesCu],[2] [Cu(NCMe)$_4$](PF_6)[3], [Cp_2Fe](PF_6)[4] and [(2,4-Br_2-C_6H_3)$_3$N](SbF_6)[5] were synthesized according to literature procedures, and K[N($SiMe_3$)$_2$] was purchased from Sigma-Aldrich Corporation. ^1H, ^{13}C, ^{31}P and ^{19}F NMR spectra were recorded with Bruker 300 MHz, 400 MHz or 500 MHz spectrometer. All chemical shifts were reported in units of ppm with references to the residual protons of the deuterated solvents for proton chemical shifts, the ^{13}C of deuterated solvents for carbon chemical shifts, the ^{19}F of $CFCl_3$ (external standard) for fluorine chemical shifts, and the ^{31}P of 85% phosphorous acid (external standard) for phosphine chemical shifts. ESI mass spectra were recorded on Bruker HCT ultra spectrometer. Elemental analyses were performed by the analytical laboratory of the Institute of Inorganic Chemistry at the University of Göttingen using an Elementar Vario EL III instrument. UV-vis spectra were recorded with an Agilent Cary 60 equipped with an Unisoku Cryostat (CoolSpek) and magnetic stirrer using quartz cuvettes with an attached tube and a screw cap with a septum. IR spectra were recorded inside a glovebox on a Cary 630 FTIR spectrometer equipped with Dial Path Technology and analyzed by FTIR MicroLab software.

Electrochemistry. Cyclic voltammetry (CV) experiments were performed in a glovebox under an argon atmosphere with an Interface 1000B potentiostat. A glassy carbon was used as working electrode, a platinum wire was used as the auxiliary electrode, and an Ag reference electrode was used as the reference electrode. 0.1 M [(*n*-Bu)$_4$N](PF_6) in CH_3CN was used as supporting electrolyte and was prepared in the glovebox. Ferrocene was used as an internal standard. The data were analyzed by Gamry Framework software.

(Spectro)electrochemistry. (Spectro)electrochemistry experiments were performed in a glovebox under an argon atmosphere with an Interface 1000B potentiostat, Deuterium/Tungsten light source (BWTEK), Exemplar LS spectrometer (BWTEK), and quartz cuvettes. A platinum mesh was used as working electrode, a platinum wire was used as the auxiliary electrode, and an Ag reference electrode was used as the reference electrode. 0.1 M [(*n*-Bu)$_4$N](PF_6) in MeCN was used as supporting electrolyte and was prepared in the glovebox. The potential was controlled by Gamry Framework software, and the data was analyzed by BWSpec software.

Magnetic Measurements. Temperature-dependent magnetic susceptibility measurements for **2** were carried out with a Quantum-Design MPMS-XL-5 SQUID magnetometer equipped with a 5 T magnet in the range from 295−2.0 K at a magnetic field of 0.5 T. The crystalline solid sample was contained in a gelatin capsule and fixed in a nonmagnetic sample holder. Each raw data file for the measured magnetic moment was corrected for the diamagnetic contribution of the capsule according to $M^{dia} = \chi_g \times m \times H$, with experimentally obtained gram susceptibilities of the capsule. The molar susceptibility data of the compounds were corrected for the diamagnetic contribution. Experimental data for **2** were modelled with the julX program[6] using a fitting procedure to the spin Hamiltonian: $\hat{H} = g\mu_B\vec{B}\cdot\vec{S}$. Temperature-independent paramagnetism (TIP = $25\cdot10^{-6}$ $cm^3\cdot mol^{-1}$) was included according to $\chi_{calc} = \chi_{exp} +$ TIP.

EPR Spectroscopy. EPR spectra were measured with a Bruker E500 ELEXSYS X-band spectrometer equipped with a standard cavity (ER4102ST, 9.45 GHz). The sample temperature was maintained constant with an Oxford instrument nitrogen flow cryostat (ESP910) and an Oxford temperature controller (ITC-4). The microwave frequency was measured with the built-in frequency counter, and the magnetic field was calibrated by using an NMR field probe (Bruker ER035M). EPR spectra were simulated using EasySpin.[7]

X-Ray Structure Determination. Crystal data and details of the data collections are given in Table S1, selected bond lengths and angles are given in Table S2, molecular structures are shown in Figures S1-S4. X-ray data were collected on a STOE IPDS II diffractometer (graphite monochromated Mo-Kα radiation, λ = 0.71073 Å) by use of scans at –140 °C. The structures were solved with SHELXT and refined on F^2 using all reflections with SHELXL-2018.[8] Non-hydrogen atoms were refined anisotropically. Hydrogen atoms were placed in calculated positions and assigned to an isotropic displacement parameter of 1.2 U_{eq}(C). Counterions in **1** (PF_6^-) and **3** (PF_6^-/SbF_6^-) were found to be disordered. In case of **3** three SbF_6^- and three PF_6^- occupy the same positions. Occupancy factors for **1** are 0.838(3) / 0.162(3), and for **3**: 0.925(2) (PF_6^-) / 0.075(2) (SbF_6^-), 0.909(2) (PF_6^-) / 0.091(2) (SbF_6^-), 0.780(7) (PF_6^-) / 0.220(7) (PF_6^-), 0.330(2) (SbF_6^-) / 0.670(2) (PF_6^-). DFIX (d_{Sb-F} = 1.86 Å), SADI ($d_{F\cdots F}$), RIGU and SAME restraints in case of **3** and EADP constraints in case of **1** and **3** were applied to model the disordered parts. Face-indexed absorption corrections were performed numerically with the program X-RED.[9]

X-Ray Spectroscopic Measurements. X-ray spectroscopic measurements were performed at beam line 6−2 at SSRL (3.0 GeV, 500 mA) in a 10 K in a liquid helium cryostat. Cu Kβ HERFD-XAS were collected using a Si(311) double crystal monochromator upstream for energy selection and a 1 m radius Johann spectrometer for the measurement of X-ray emission equipped with seven Si(531) analyzer crystals and a silicon-drift detector windowed to Kβ emission region. The incident energy was calibrated to the first inflection point of a Cu reference foil set to an energy of 8980.3 eV. The emission spectrometer was calibrated with numerous elastic scattering scans throughout the Cu Kβ emission region post monochromator calibration. A beam size of approximately 400 (h) x 100 (v) μm was used. Cu Kβ HERFD-XAS was collected by selection at the maximum of the Cu Kβ emission spectrum (~8904 eV) and sweeping the incident energy on a fresh sample spot. Data was collected in 0.25 eV step sizes in the XANES region (8976 to 9000 eV) and a larger 1.0 eV step sizes below 8976 eV and above 9000 eV. All samples were monitored for radiation damage by evaluation of the pre-edge (when present) and the edge energies and structures. The sample exposure time was limited and incident flux was attenuated to eliminate the observation of radiation damage and optimize data collection conditions.

All data was processed in an equivalent manner in Matlab (Mathworks Inc.). The averaged scans were normalized for an edge-jump of 1. Pre-edge features were fit by subtraction of the edge region from the pre-edge region by constraining a single pseudo-Voigt line shape to the pre-edge region and fitting the XANES region to multiple pseudo-Voigt line shapes, similar to previously described methods.[10]

Computational Details. The ORCA program package (version 3.0.3) was employed for all calculations.[11] Geometry optimization of the cations were performed starting from the crystallographic data of **1−3** (BP86 functional, def2-tzvp basis set,[12] RI approximation using the auxiliary def2-tzvp/J basis set, D3 dispersion correction with Becke-Johnson damping,[13] tight convergence and optimization criteria) at different spin states (spin restricted calculations in case of closed-shell molecules, otherwise spin unrestricted calculations, unless otherwise stated). Single point energies were calculated on the optimized coordinates by using B3LYP functional and the RIJCOSX approximation with the same basis sets and dispersion correction as stated above. The relative energies and selected bond lengths are given in Table 2. The transition state of **1** was calculated using the OptTS feature of ORCA. A single imaginary frequency at −33.97 cm^{-1} was found for the transition state. TD-DFT calculations were carried out at the B3LYP/def2-tzvp level of theory (number of roots = 80) as well as the Broken-Symmetry calculations. The coupling constant J, was calculated according to Yamaguchi.[14] XAS spectra were calculated in ORCA (v 4.1) as previously reported[10] via application of time-dependent density functional theory (TDDFT) using the BP86 optimized geometries, but employing the PBE0 functional. The calculation was limited to the pre-edge region with 150 roots calculated. All spectra were broadened with a Gaussian line shape of 1.4 eV (FWHM).

Preparation of [LCu](PF$_6$) (1). *Method A*: At room temperature, to a MeCN (30 mL) solution of $[H_2L](PF_6)_2$ (740 mg, 1.16 mmol) was slowly added mesitylcopper (440 mg, 2.41 mmol). The suspension was heated to 60 °C for one week, and during this time the color of the suspension changed from white to yellow. After filtration, the resulting yellow solid was washed with THF or Et_2O (2 mL × 3) and dried under vacuum to leave **1** as a yellow powder (420 mg, 66%). *Method B*: At −35 °C, to a MeCN (20 mL) solution of $[H_2L](PF_6)_2$ (400 mg, 0.63 mmol) was slowly added $K[N(SiMe_3)_2]$ (251 mg, 1.26 mmol). The color of the solution changed from colorless to red immediately. Then $[Cu(NCMe)_4](PF_6)$ (235 mg, 0.63 mmol) was added, and the color of the solution changed from red to yellow quickly along with the generation of a white precipitate. The reaction mixture was warmed to 60 °C and stirred for one week, and during this time the white precipitate disappeared and the formation of a yellow precipitate was observed. After filtration, the resulting yellow solid was washed with THF (2 mL × 3) and dried under vacuum to give **1** as a yellow powder (230 mg, 66%). Single-crystals of **1** suitable for X-ray diffraction studies were grown by diffusing Et_2O into a saturated MeCN solution at room temperature. ^1H NMR (400 MHz, $[D_3]$MeCN, 298 K): δ (ppm) 7.75 (t, J = 7.6 Hz, 2H, C*H*-*p*-Py), 7.34 (d, J = 7.6 Hz, 4H, C*H*-*m*-Py), 6.96 (s, 4H, C*H*-imidazolyl backbone), 5.20 (s, 8H, C*H$_2$*-linkers). ^{13}C NMR (100 MHz, $[D_3]$MeCN, 298 K): δ (ppm) 177.4 (*N*CN), 154.9 (*C*H-*o*-Py), 138.7 (*C*H-*p*-Py), 122.9 (*C*H-*m*-Py), 121.7 (*C*H-imidazolyl backbone), 55.2 (CH_2-linkers). ^{19}F NMR (283 MHz, $[D_3]$MeCN, 298 K): δ (ppm) −72.9 (d, $J_{P\text{-}F}$ = 708.1 Hz). ^{31}P NMR (122 MHz, $[D_3]$MeCN, 298 K): δ (ppm) −144.6 (hepta, $J_{F\text{-}P}$ = 709.3 Hz). Anal. Calcd. for $C_{20}H_{18}CuN_6PF_6$: C 43.60, H 3.29, N 15.25; Found: C 43.72, H 3.35, N 15.26. ESI–MS (MeCN) m/z (%): 405.1 (100) $[CuC_{20}H_{18}N_6]^+$. Absorption spectrum (in CH_3CN): λ_{max}, nm (ε, $M^{-1}\cdot cm^{-1}$) 260 (15670), 280 (13580), 340 (4960). ATR−IR (powder, cm^{-1}): v = 3129 (w), 1594 (w), 1578 (w), 1570 (w), 1560 (w), 1463 (w), 1452 (w), 1409 (w), 1390 (w), 1328(w), 1287 (w), 1267 (w), 1240 (w), 1200(w), 1164 (w), 1111 (w), 1095 (w), 1089 (w), 999 (w), 943 (w), 934 (w), 876 (w), 845 (s), 826 (s), 775 (m), 758 (m), 750 (m), 731 (m), 721 (s), 672 (m), 606 (m), 555 (s), 443 (w). Few colorless crystals that turned out to be the dinuclear complex $[L_2Cu_2](PF_6)_2$ (**1′**) were also formed during the crystallization.

Preparation of [L$_2$Cu$_2$](PF$_6$)$_2$ (1′). During the synthesis of complex **1** via method B, a white precipitate was generated after the addition of $[Cu(NCMe)_4](PF_6)$. The white precipitate was collected by filtration, washed with THF (2 mL) and dried under vacuum to give **1′** as a white solid. The IR (solid) spectrum of this white solid is essentially identical with the spectrum of the colorless crystals of **1′** obtained during the crystallization of **1**. ATR−IR (powder, cm^{-1}): v = 3178 (w), 3152 (w), 1600 (w), 1578 (w), 1571 (w), 1457 (w), 1432 (w), 1420 (w), 1375 (w),1361 (w), 1346 (w), 1252 (w),1243(w), 1207 (w), 1193 (w), 1176 (w), 1167 (w), 1157 (w), 1124 (w), 1114 (w), 1101 (w), 1094 (w), 1051 (w), 1032 (w), 996 (w), 992 (w), 949 (w), 877 (w), 852 (m), 834 (s), 784 (m), 756 (m), 734 (s), 712 (w), 666 (w), 657 (w), 642 (w), 634 (w), 611 (w), 604 (w), 592 (w), 556 (s), 527 (w), 482 (w), 453 (w). Further characterization of **1′** in solution state was not possible due to the immediate conversion into **1** in solution.

Preparation of [LCu](PF$_6$)$_2$ (2). At −35 °C, to a MeCN (5 mL) solution of $[LCu](PF_6)$ (**1**, 120 mg, 0.22 mmol) was slowly added $[Cp_2Fe](PF_6)$ (72 mg, 0.22 mmol). The color of the solution changed from yellow to red immediately. The reaction mixture was stirred for 30 min at room temperature and then subjected to vacuum to remove all the volatiles. The resulting red solid was washed with *n*-hexanes (3 mL × 3) until the washing liquid becomes almost colorless, then extracted with MeCN (3 mL) and filtered. The red crystals of **2** (139 mg, 86%) were obtained by slow diffusion of Et_2O to this MeCN solution at room temperature. Anal. Calcd. for $C_{20}H_{18}CuN_6P_2F_{12}$: C 34.52, H 2.61, N 12.08; Found: C 34.62, H 2.39, N 12.08 (The coordinated MeCN has been removed after 12 h under high vacuum). ESI–MS (MeCN) m/z (%): 549.9 (100) $[C_{20}H_{18}CuN_6PF_6]^+$, 202.2 (78%) $[C_{20}H_{18}CuN_6]^{2+}$. Absorption spectrum (in CH_3CN): λ_{max}, nm (ε, $M^{-1}\cdot cm^{-1}$) 260 (18230), 370 (220), 490 (120). ATR−IR (powder, cm^{-1}): v = 3152 (w), 1601 (w), 1577 (w), 1568 (w), 1491 (w), 1451 (w), 1439 (w), 1427 (w), 1385 (w), 1345(w), 1323 (w), 1284 (w), 1270 (w), 1205 (w), 1185 (w), 1175 (w), 1115 (w), 1058 (w), 1006 (w), 982 (w), 971 (w), 942 (w), 911 (w), 824 (s), 781 (s), 765 (s), 736 (s), 657 (m), 626 (m), 613 (m), 599 (m), 554 (s), 409 (w) (no peak due to MeCN around 2200 cm^{-1} was observed, indicating the removal of CH_3CN under high vacuum).

Preparation of [LCu](PF_6)$_2$(SbF_6) (3). At −35 ^{o}C, to a MeCN (2 mL) solution of [LCu](PF_6)$_2$ (**2**, 81 mg, 0.11 mmol) was slowly added [2,4-Br_2-C_6H_3](SbF_6) (104 mg, 0.11 mmol). The color of the solution changed from red to dark-red immediately. The reaction mixture was stirred for 30 min at room temperature, and was then filtered. Dark-red crystals of **3** were obtained by slow diffusion of Et_2O into the filtrate at room temperature. After recrystallizing twice, **3** was obtained in good purity (60 mg, 60%). ^{1}H NMR (500 MHz, [D$_3$]MeCN, 298 K): *δ* (ppm) 8.44 (t, *J* = 7.5 Hz, 2H, C*H*-*p*-Py), 8.07 (d, *J* = 7.6 Hz, 4H, C*H*-*m*-Py), 7.67 (s, 4H, C*H*-imidazolyl backbone), 5.97 (s, 8H, C*H$_2$*-linkers). ^{1}H NMR (400 MHz, [D$_6$]acetone, 298 K): *δ* (ppm) 8.71 (t, *J* = 7.6 Hz, 2H, C*H*-*p*-Py), 8.41 (d, *J* = 7.6 Hz, 4H, C*H*-*m*-Py), 8.03 (s, 4H, C*H*-imidazolyl backbone), 6.45/6.02 (ABq, 8H, *J* = 16.8 Hz, C*H$_2$*-linkers). ^{13}C NMR (125 MHz, [D$_3$]MeCN, 298 K): *δ* (ppm) 153.7 (*C*H-*o*-Py), 151.8 (N*C*N), 145.6 (*C*H-*p*-Py), 131.1 (*C*H-*m*-Py), 125.5 (*C*H-imidazolyl backbone), 55.7 (*C*H$_2$-linkers). ^{19}F NMR (471 MHz, [D$_3$]MeCN, 298 K): *δ* (ppm) −72.7 (d, $J_{P\text{-}F}$ = 707.4 Hz), no ^{19}F signal of [SbF_6] was observed, possibly due to the $^{121/123}$Sb (I = 5/2, 7/2) nuclei. ^{31}P NMR (203 MHz, [D$_3$]MeCN, 298 K): *δ* (ppm) −144.6 (hepta, $J_{F\text{-}P}$ = 708.7 Hz). Anal. Calcd. for $C_{20}H_{18}CuN_6P_{2.75}Sb_{0.25}F_{18}$: C 27.82, H 2.10, N 9.73; Found: C 28.08, H 2.18, N 9.95 (The found elemental analysis data is consistent with the composition observed by X-ray diffraction analysis, assuming that the coordinated MeCN has been removed after 12 h under high vacuum). Absorption spectrum (in MeCN): λ_{max}, nm (*ε*, M^{-1}· cm^{-1}) 260 (25460), 300 (6900), 350 (2900), 530 (290). ATR−IR (powder, cm^{-1}): *v* = 3169 (w), 3148 (w), 1604 (w), 1567 (w), 1530 (w), 1470 (w), 1443 (w), 1383 (w), 1334 (w), 1266 (w), 1219 (w), 1190 (w), 1179 (w), 1115 (w), 1078(w), 815 (s), 782 (s), 737 (s), 658 (m), 553 (s), 453 (w), 431 (w) (no peak due to MeCN around 2200 cm^{-1} was observed, indicating the removal of MeCN under high vacuum).

1. Crystallographic Data

Table S1. Crystal data and refinement details for **1**, **2**, and **3**.

Compound	**1(ly055)**	**1′(yl9)**	**2(yl3)**	**3(yl5)**
empirical formula	$C_{20}H_{18}CuF_6N_6P$	$C_{40}H_{36}Cu_2F_{12}N_{12}P_2$	$C_{24}H_{24}CuF_{12}N_8P_2$	$C_{52}H_{54}Cu_2F_{36}N_{18}P_{5.50}Sb_{0.50}$
moiety formula	$C_{20}H_{18}CuN_6^+$, F_6P^-	$C_{40}H_{36}Cu_2N_{12}^{2+}$, $2(F_6P^-)$	$C_{22}H_{21}CuN_7^{2+}$, $2(F_6P^-)$, C_2H_3N	$2(C_{22}H_{21}CuN_7^{3+})$, $5.5(F_6P^-)$, $0.5(F_6Sb^-)$, $4(C_2H_3N)$
formula weight	550.91	1101.83	777.99	1973.01
crystal size [mm³]	0.50 x 0.24 x 0.14	0.24 x 0.13 x 0.10	0.50 x 0.19 x 0.16	0.50 x 0.37 x 0.26
crystal system	triclinic	Orthorhombic	orthorhombic	triclinic
space group	*P*–1 (No. 2)	*Pbcn* (No. 60)	*Pbca* (No. 61)	*P*–1 (No. 2)
a [Å]	9.5890(5)	23.3578(9)	8.74300(10)	11.3010(3)
b [Å]	10.0003(5)	11.4032(5)	18.0411(4)	16.8936(5)
c [Å]	11.3343(5)	16.3860(8)	37.1179(6)	20.2152(6)
α [°]	105.425(4)	90	90	76.107(2)
β [°]	92.439(4)	90	90	78.407(2)
γ [°]	91.778(4)	90	90	87.214(2)
V [Å³]	1045.77(9)	4364.5(3)	5854.73(17)	3670.05(19)
Z	2	4	8	2
ρ [g·cm⁻³]	1.750	1.677	1.765	1.785
F(000)	556	2224	3128	1964
μ [mm⁻¹]	1.197	1.147	0.965	1.021
T_{min} / T_{max}	0.4032 / 0.5806	0.7172 / 0.9000	0.8660 / 0.9771	0.5261 / 0.8545
θ–range [°]	1.866 – 26.734	1.744 – 26.869	2.195 – 25.721	1.242 – 25.804
hkl–range	±12, ±12, –13 to 14	±29, ±14, −20 to 18	–10 to 9, ±21, ±45	±13, ±20, ±24
measured refl.	14943	21866	62081	45366
unique refl. [R_{int}]	4438 [0.0282]	4651 [0.1000]	5537 [0.0562]	13830 [0.0534]
obs. refl. ($I > 2\sigma(I)$)	3981	2806	4433	12181
data / restr. / param.	4438 / 0 / 329	4651 / 0 / 307	5537 / 0 / 426	13830 / 921 / 1271
goodness–of–fit (F^2)	1.050	1.022	1.043	1.048
*R*1, *wR*2 ($I > 2\sigma(I)$)	0.0328 / 0.0845	0.0449 / 0.0895	0.0397 / 0.0980	0.0555 / 0.1521
*R*1, *wR*2 (all data)	0.0379 / 0.0876	0.0992 / 0.1080	0.0536 / 0.1091	0.0623 / 0.1588
res. el. dens. [e·Å⁻³]	–0.461 / 0.629	−0.323 / 0.435	–0.365 / 0.596	–0.941 / 2.536

Table S2. Selected distances [Å] and angles [°].

	1	**1′**	**2**	**3**[a]
Cu–C	1.939(2) / 1.946(2)	1.896(3)/1.896(3)	1.907(3) / 1.909(3)	1.875(4) / 1.880(4) 1.868(4) / 1.868(4)
Cu–N^{py}	2.496(2) / 2.706(2)		2.155(2) / 2.157(3)	1.972(3) / 1.974(3) 1.964(3) / 1.974(3)
Cu–N^{MeCN}	-		2.321(3)	2.325(4) / 2.315(4)
C–Cu–C	169.62(8)	168.34(15)	168.42(13)	173.36(17) / 172.55(17)
N^{py}–Cu– N^{py}	164.49(5)		169.83(9)	173.14(13) / 172.25(13)
Cu–N–C^{MeCN}	-		173.8(3)	160.7(4) / 165.9(4)

[a] The asymmetric unit contains two crystallographically independent molecules.

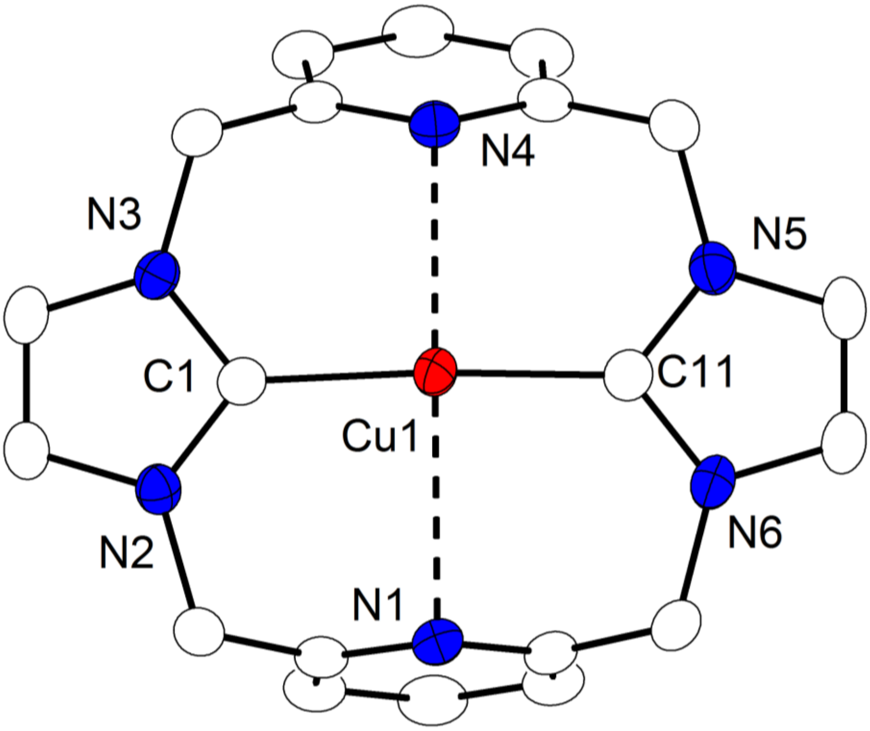

Figure S1. Plot (50% probability thermal ellipsoids) of the molecular structure of the cationic part of **1** (hydrogen atoms omitted for clarity). Selected bond lengths [Å] and angles [°]: Cu1–C1 1.939(2), Cu1–C11 1.946(2), Cu1–N1 2.7064(17), Cu1–N4 2.4958(17); C1–Cu1–C11 169.62(8), C1–Cu1–N4 92.15(7), C11–Cu1–N4 90.01(8), C1–Cu1–N1 87.48(7), C11–Cu1–N1 87.73(7), N4–Cu1–N1 164.49(5).

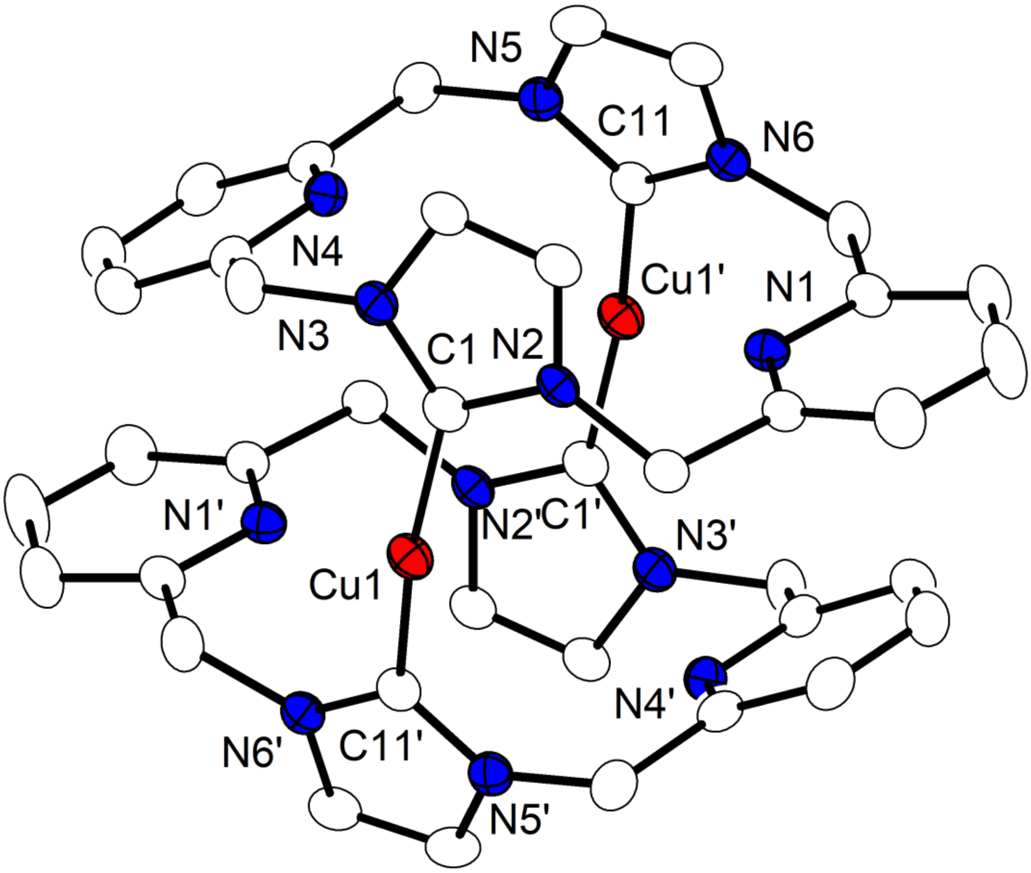

Figure S2. Plot (50% probability thermal ellipsoids) of the molecular structure of the cationic part of **1′** (hydrogen atoms omitted for clarity). Selected bond lengths [Å] and angles [°]: Cu1–C1 1.896(3), Cu1–C11′ 1.896(3), Cu1···Cu1′ 5.3486(7); C1–Cu1–C11′ 168.34(15). Symmetry transformation used to generate equivalent atoms: (′) 1-*x*, 1-*y*, 1-*z*. Note: There is a rather short intermolecular Cu···Cu distance of 2.8679(8) Å.

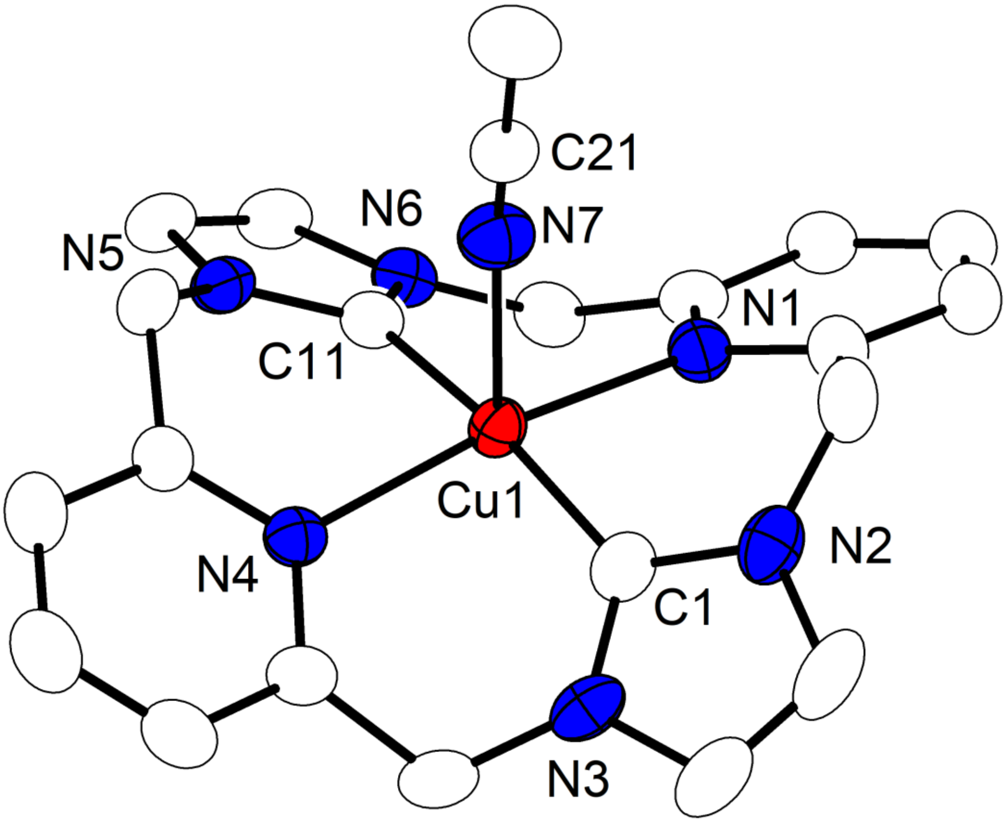

Figure S3. Plot (50% probability thermal ellipsoids) of the molecular structure of the cationic part of **2** (hydrogen atoms omitted for clarity). Selected bond lengths [Å] and angles [°]: Cu1–C1 1.909(3), Cu1–C11 1.907(3), Cu1–N1 2.157(3), Cu1–N4 2.155(2), Cu1–N7 2.321(3); C11–Cu1–C1 168.42(13), C11–Cu1–N4 89.37(11), C1–Cu1–N4 89.84(12), C11–Cu1–N1 89.84(11), C1–Cu1–N1 88.91(12), N4–Cu1–N1 169.83(9), C11–Cu1–N7 95.73(11), C1–Cu1–N7 95.85(11), N4–Cu1–N7 93.34(10), N1–Cu1–N7 96.83(10), C21–N7–Cu1 173.8(3).

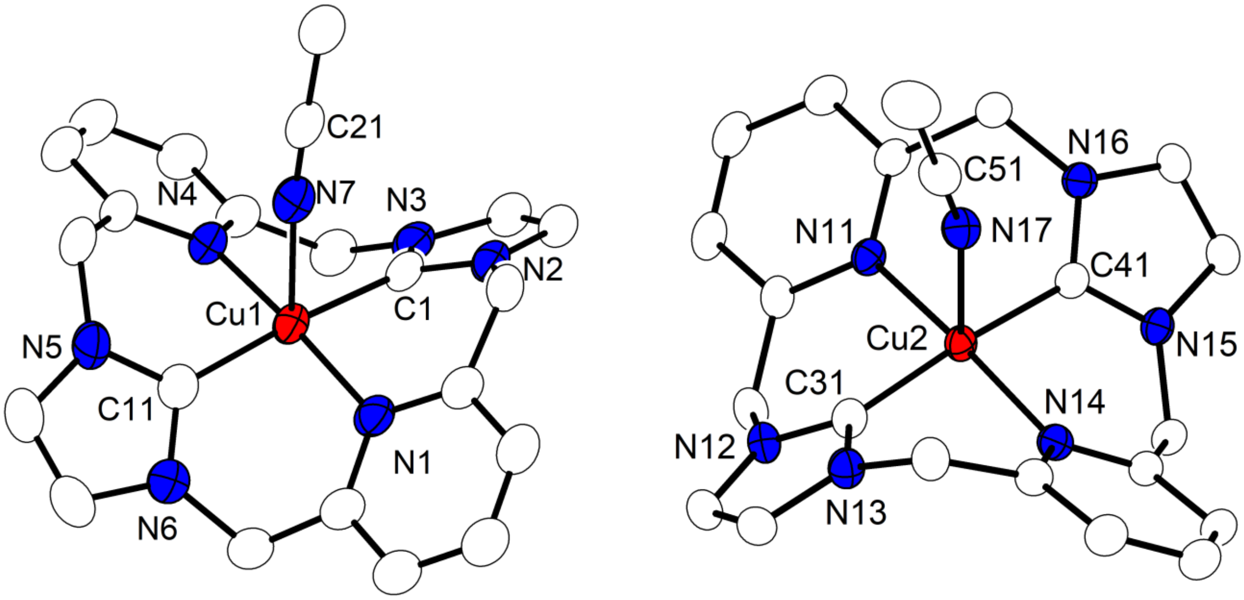

Figure S4. Plot (50% probability thermal ellipsoids) of the molecular structure of the cationic part of **3** (left) and **3′** (right) (hydrogen atoms omitted for clarity; **3** and **3′** are two crystallographically independent molecules in the asymmetric unit). Selected distances [Å] and angles [°]: Cu1–C1 1.880(4), Cu1–C11 1.875(4), Cu1–N1 1.974(3), Cu1–N4 1.972(3), Cu1–N7 2.325(4), Cu2–C31 1.868(4), Cu2–C41 1.868(4), Cu2–N11 1.964(3), Cu2–N14 1.974(3), Cu2–N17 2.315(4); C1–Cu1–C11 173.36(17), C1–Cu1–N4 90.72(15), C1–Cu1–N1 88.93(15), C11–Cu1–N4 88.86(16), C11–Cu1–N1 90.69(16), N4–Cu1–N1 173.14(13), C1–Cu1–N7 89.64(15), C11–Cu1–N7 96.99(15), N1–Cu1–N7 96.19(13), N4–Cu1–N7 90.66(13), C21–N7–Cu1 160.7(4), C31–Cu2–C41 172.55(17), C31–Cu2–N14 88.79(16), C41–Cu2–N14 90.79(15), C31–Cu2–N11 91.55(15), C41–Cu2–N11 87.87(15), N11–Cu2–N14 172.25(13), C31–Cu2–N17 93.19(15), C41–Cu2–N17 94.26(15), N14–Cu2–N17 94.30(13), N11–Cu2–N17 93.41 (13), C51–N17–Cu2 165.9(4).

2. Equilibrium between 1 and 1′

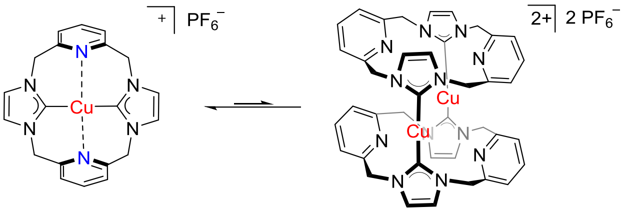

[LCu](PF$_6$) (**1**)

[L$_2$Cu$_2$](PF$_6$)$_2$ (**1**′)

Scheme 1. The equilibrium between the monomer (**1**) and dimer (**1′**).

Solid samples of **1** and **1′** show different IR spectra (Figures S8 and S9). However, a yellow solution is obtained when **1′** is dissolved in MeCN, and the ^{1}H NMR, UV-vis, and MS(ESI) spectra of **1′** in MeCN (at room temperature) are the same as those recorded for **1**. When **1′** was added to frozen [D$_3$]MeCN and [D$_6$]acetone in J. Young NMR tubes, respectively, and ^{1}H NMR spectrum were immediately recorded at −40 °C and −85 °C (respectively), the spectra are identical with those of **1** recorded at the same temperatures. It is noteworthy that the ^{1}H NMR spectra of **1** and **1′** in [D$_3$]MeCN at −40 °C show a series of new peaks with low intensity (Figure S42). A ^{1}H-DOSY experiment shows that these new peaks belong to different species with diffusion constants smaller than the one of **1**, which is an indication of their higher molecular weight (Figure S43). Attempts to clearly assign these new peaks through 2D-NMR experiments were unsuccessful due to the weakness of these peaks. These data suggest that the monomeric form **1** is the most dominant form in solution, and that the equilibrium between the monomer (**1**) and the dimer (**1′**) and/or other oligomers is quite fast.

3. UV-vis Spectra of 1-3

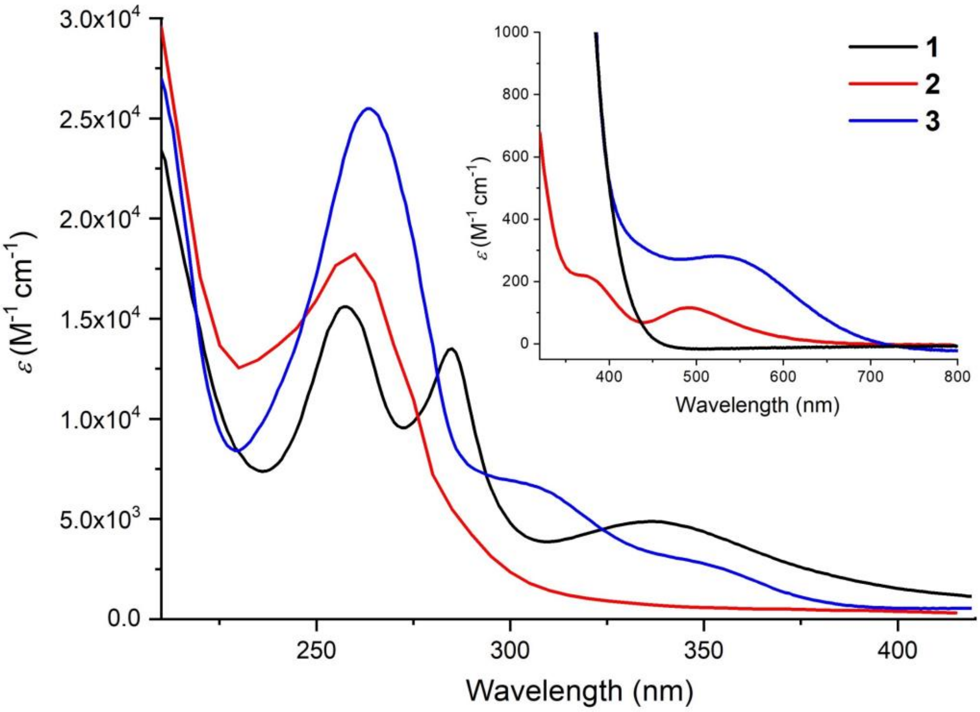

Figure S5. UV-vis spectra of **1**–**3** (in MeCN) recorded at room temperature.

Table S3. Absorption spectra data of **1**–**3** (in MeCN) recorded at room temperature.

Complexes	λ_{max}, nm (ε, $M^{-1} cm^{-1}$)
1	260 (15670), 280 (13580), 340 (4960)
2	260 (18230), 370 (220), 490 (120)
3	260 (25460), 300 (6900), 350 (2900), 530 (290)

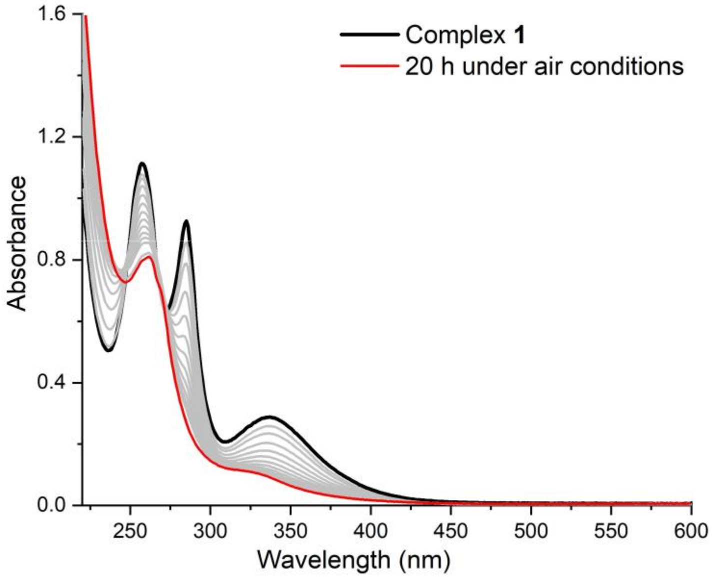

Figure S6. UV-vis spectra of **1** (in MeCN) under air conditions recorded at room temperature (the decomposition of **1** through grey lines is visible).

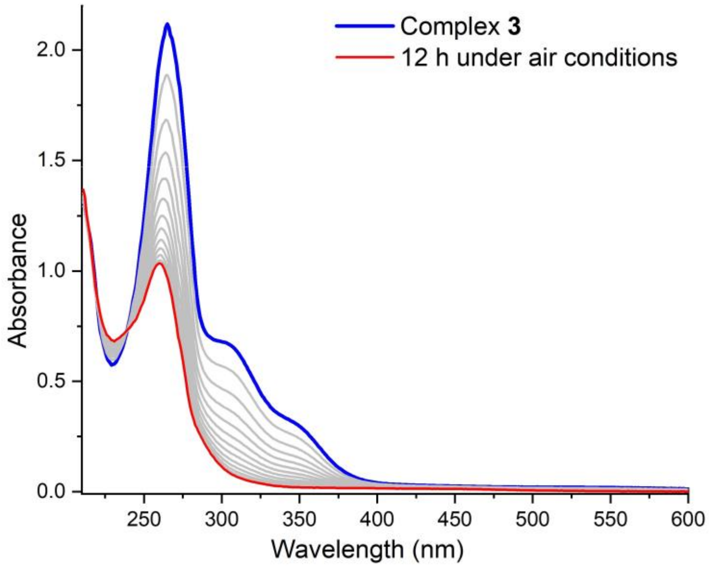

Figure S7. UV-vis spectra of **3** (in MeCN) under air conditions recorded at room temperature (the decomposition of **3** through grey lines is visible).

4. IR Spectra of 1-3

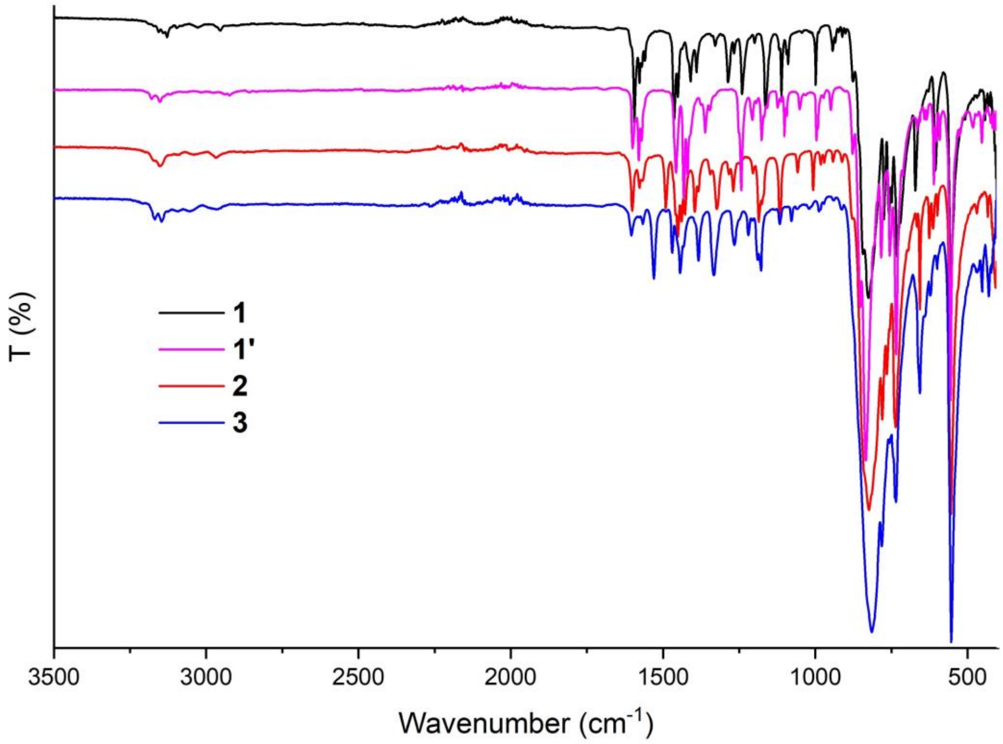

Figure S8. Comparative ATR–IR spectra of **1**, **1′**, **2** and **3** (solid, wavenumber range from 3500 to 400 cm^{-1}).

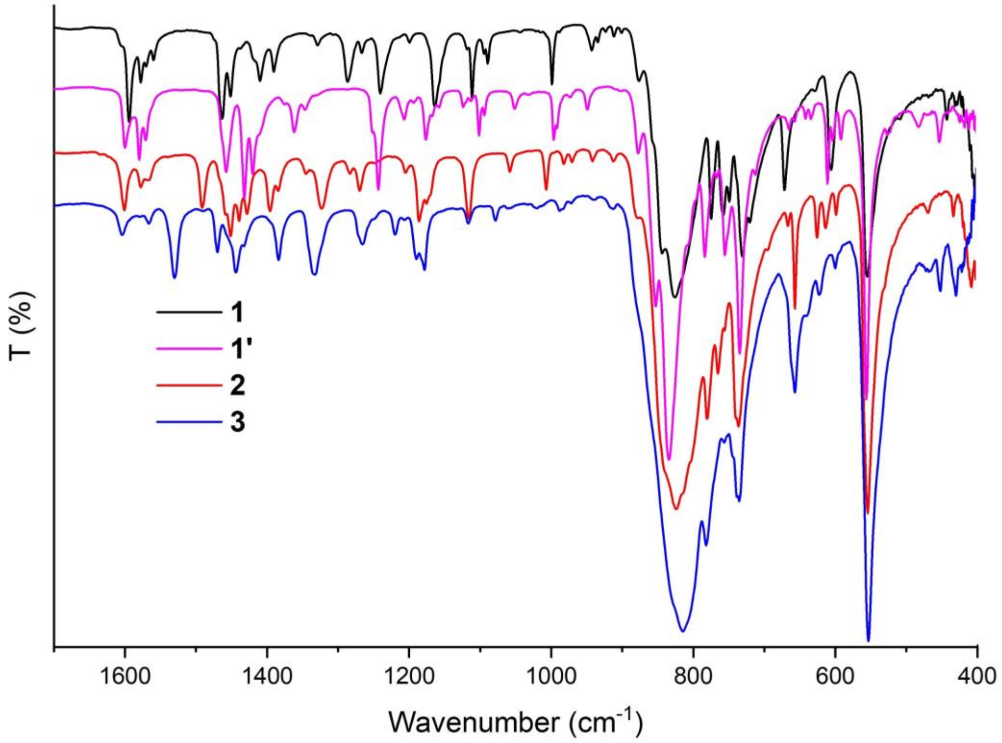

Figure S9. Comparative ATR-IR spectra of **1**, **1′**, **2** and **3** (solid, wavenumber range from 1700 to 400 cm^{-1}).

5. ESI Mass Spectra of 1 and 2

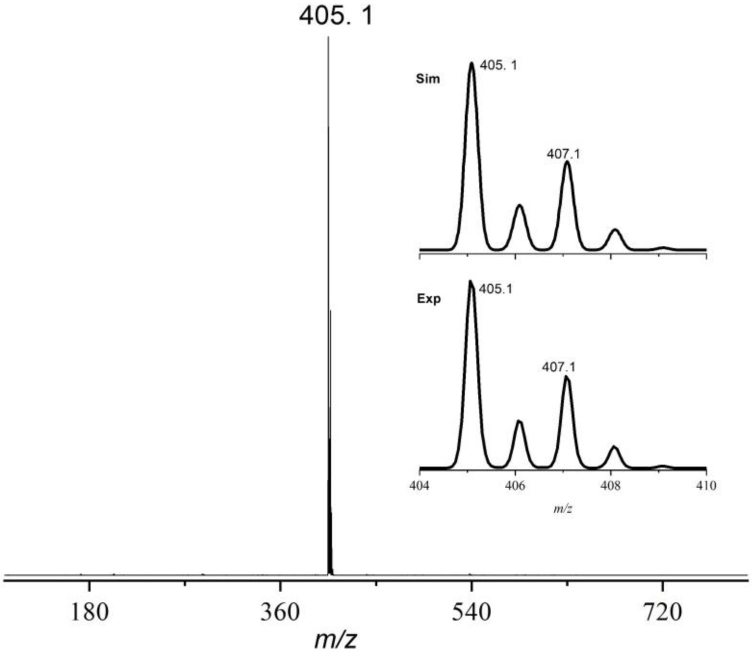

Figure S10. ESI–MS of complex **1** in MeCN. The inset shows the experimental (bottom) and simulated (top) isotope pattern for the peak around *m*/*z* = 405 (100) $[M-PF_6]^+$.

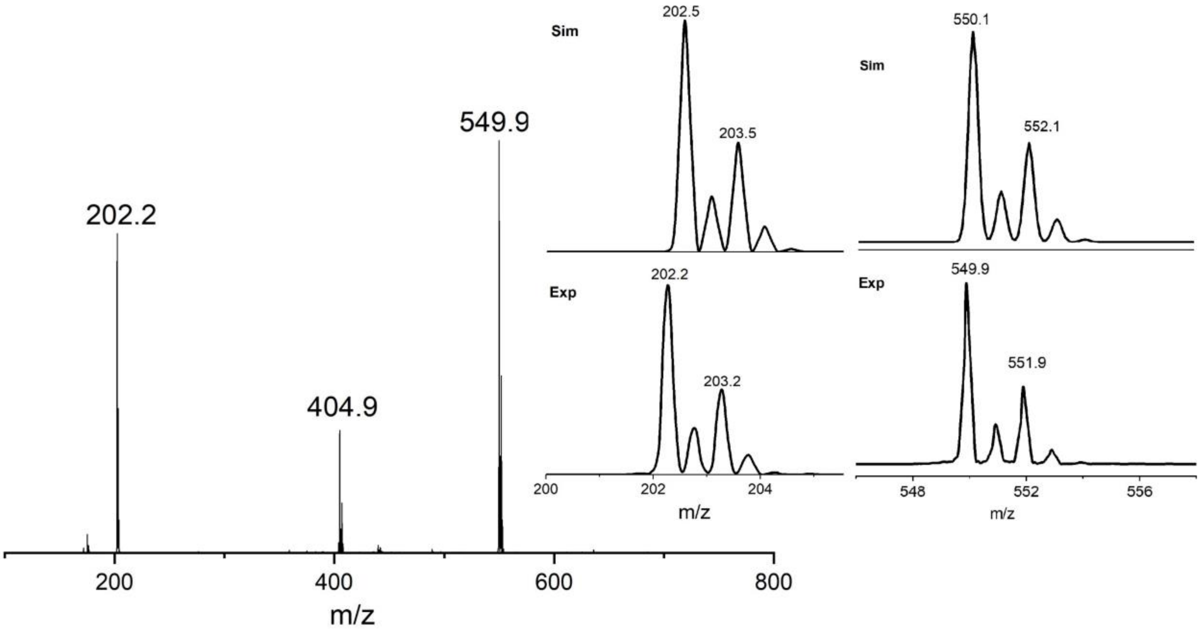

Figure S11. ESI–MS of complex **2** in MeCN. The inset shows the experimental (bottom) and simulated (top) isotope pattern for the peak around *m*/*z* = 202 (78), $[M-2PF_6]^{2+}$ and *m*/*z* = 550 (100), $[M-PF_6]^+$. The peak around *m*/*z* = 405 (30) can be attributed to the cation of **1**, which likely originates from the reduction of **2** during the ionization process.

6. Cyclic Voltammetry of 1

Cyclic voltammetry experiments were performed using ferrocene as the internal standard. Under the experimental conditions the Fc/Fc$^+$ couple is a reversible redox couple showing a peak separation of ΔE^p = 76 mV (100 mV/s) with a slight dependence on the scan rate. Due to the electrode-absorption of the copper species, the working electrode was polished after each scan cycle, however, the broadening of return peaks still can be observed.

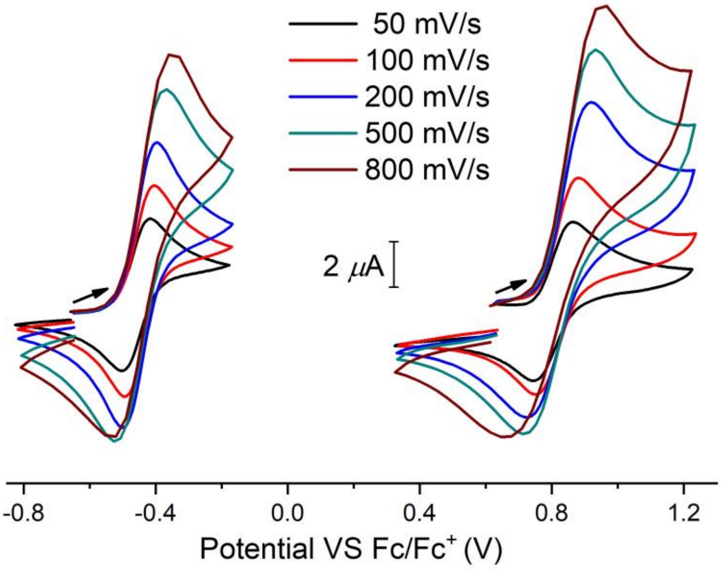

Figure S12. Cyclic voltammograms of **1** in MeCN (0.1 M ^{n}Bu$_4$NPF$_6$) at different scan rates. Left: Cu^I/Cu^{II} redox couple; Right: Cu^{II}/Cu^{III} redox couple.

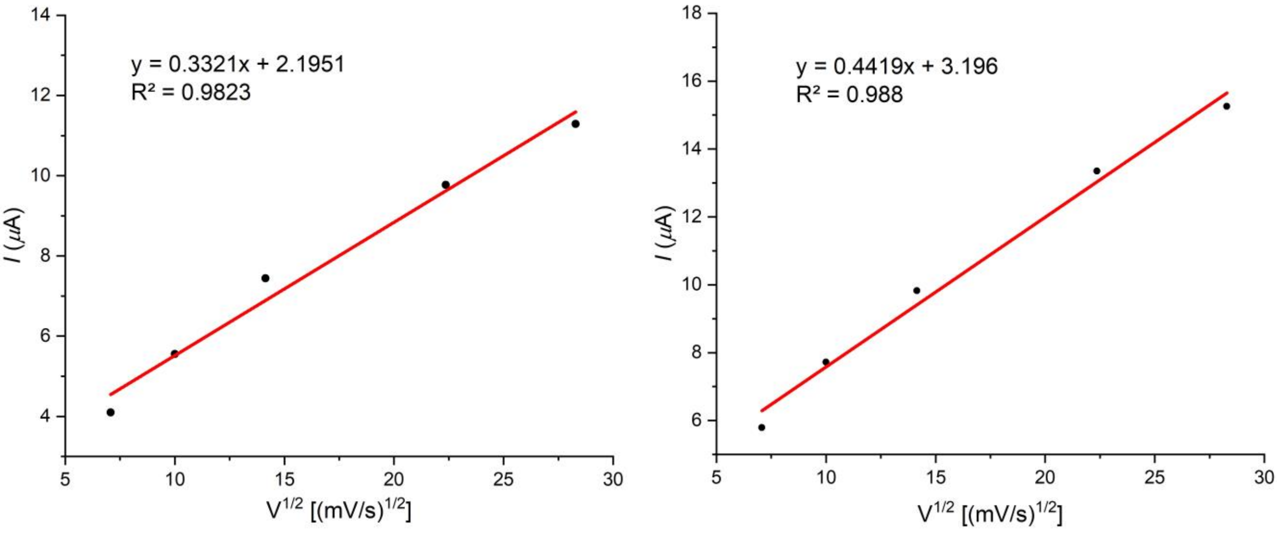

Figure S13. Linear dependence of the current I_{fp} of the forward peak on the square root of the scan rate. Left: Cu^I/Cu^{II} redox couple; Right: Cu^{II}/Cu^{III} redox couple.

7. EPR spectrum of 2 at 147 K

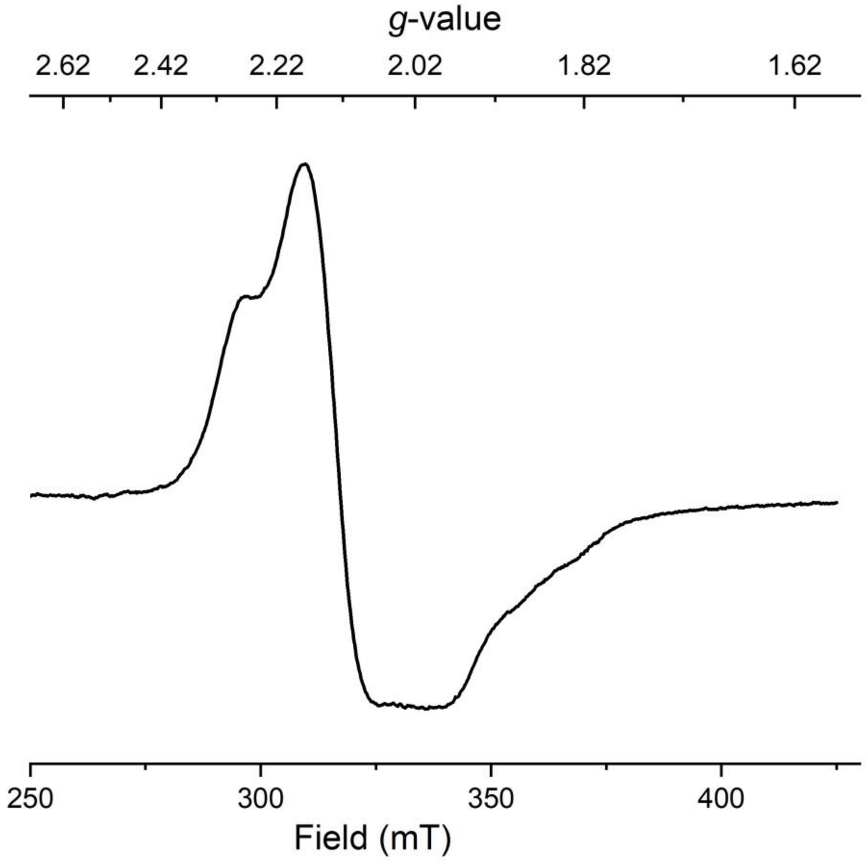

Figure S14. EPR spectrum of **2** recorded in frozen MeCN solution at 147 K. Instrumental parameters: *v* = 9.427 GHz, modulation frequency = 100 kHz, modulation amplitude = 4.0 G, microwave power = 7.95 mW, conversion time = 5.12 ms, time constant = 40.96 ms, sweep time = 5.24 s. The spectrum exhibits a rhombic signal with approximate *g*-values [2.25, 2.12, 2.00], however, it could not be satisfactorily simulated due to the rather large linewidths.

8. SQUID Magnetometry of 2

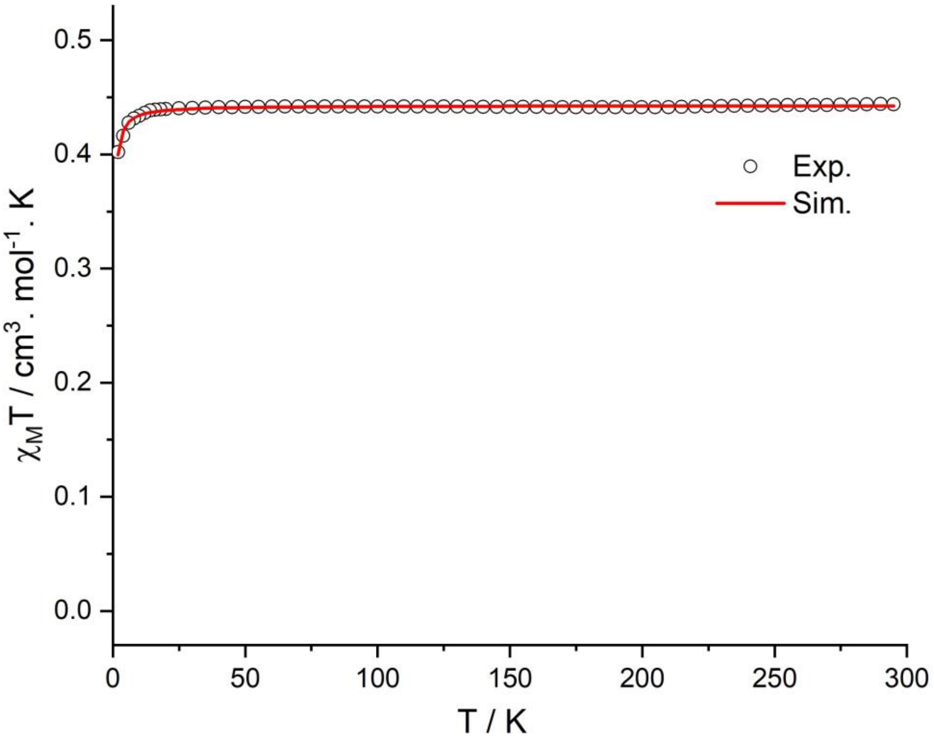

Figure S15. $\chi_M T$ vs. T measurement for a solid sample of **2** in the temperature range of 295 – 2 K at 0.5 T. Best fit parameters for the simulation with $S = ½$ are $g = 2.17$ and $TIP = 25\cdot10^{-6}$ $cm^3\cdot mol^{-1}$. Weak intermolecular interactions were considered in a mean field approach by using a Weiss temperature $\Theta = -0.2$ K.

9. NMR Spectra

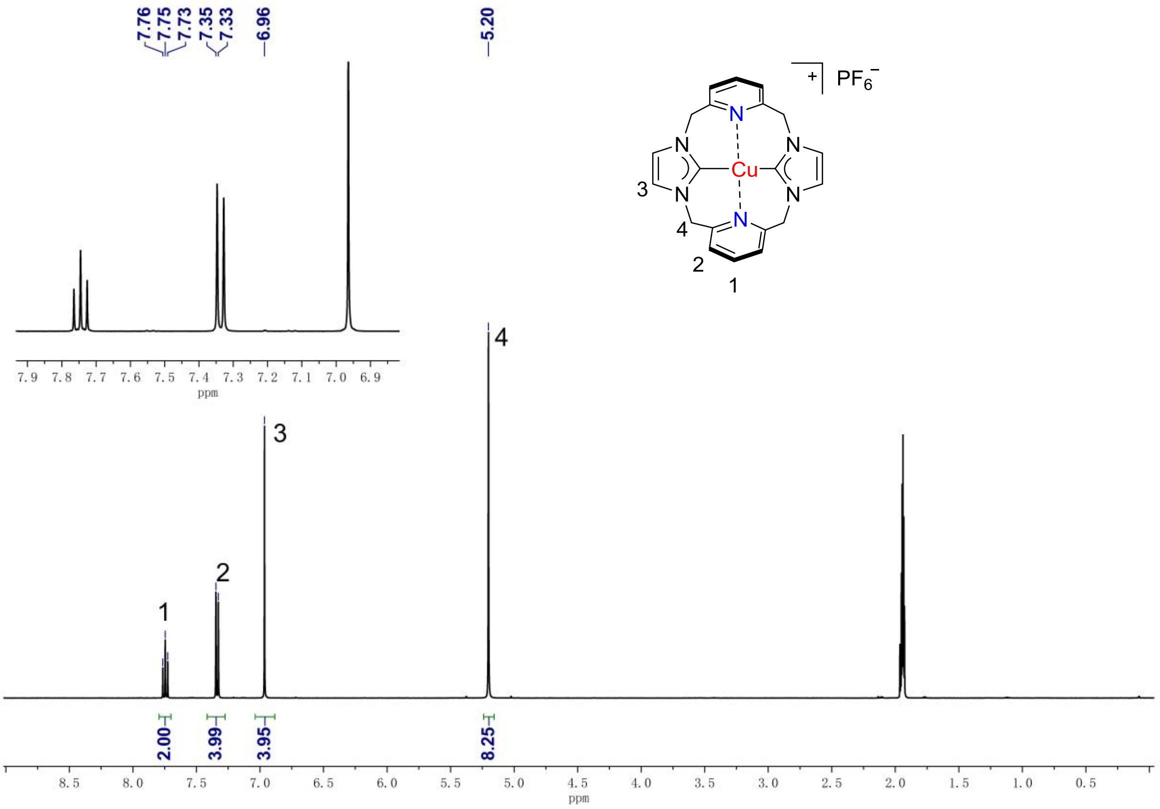

Figure S16. ^{1}H NMR spectrum of [LCu](PF$_6$) (**1**) in [D$_3$]MeCN (400 MHz, 298 K).

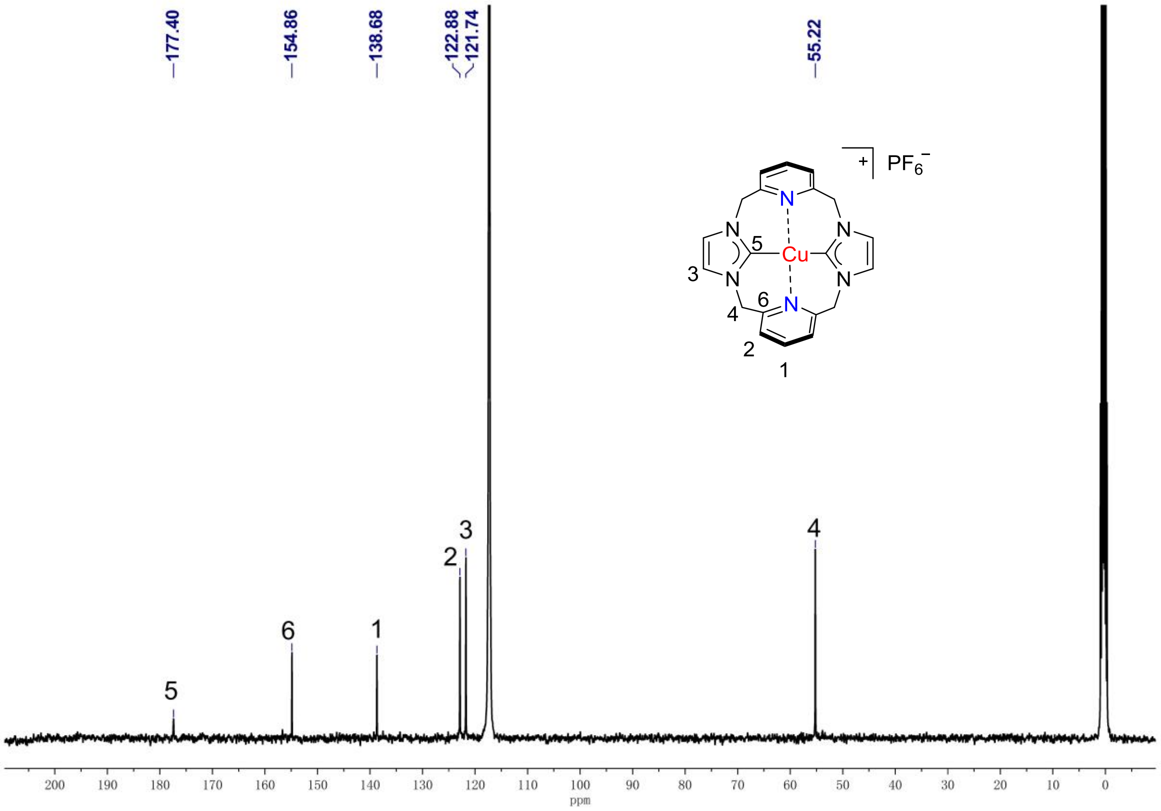

Figure S17. ^{13}C NMR spectrum of [LCu](PF$_6$) (**1**) in [D$_3$]MeCN (100 MHz, 298 K).

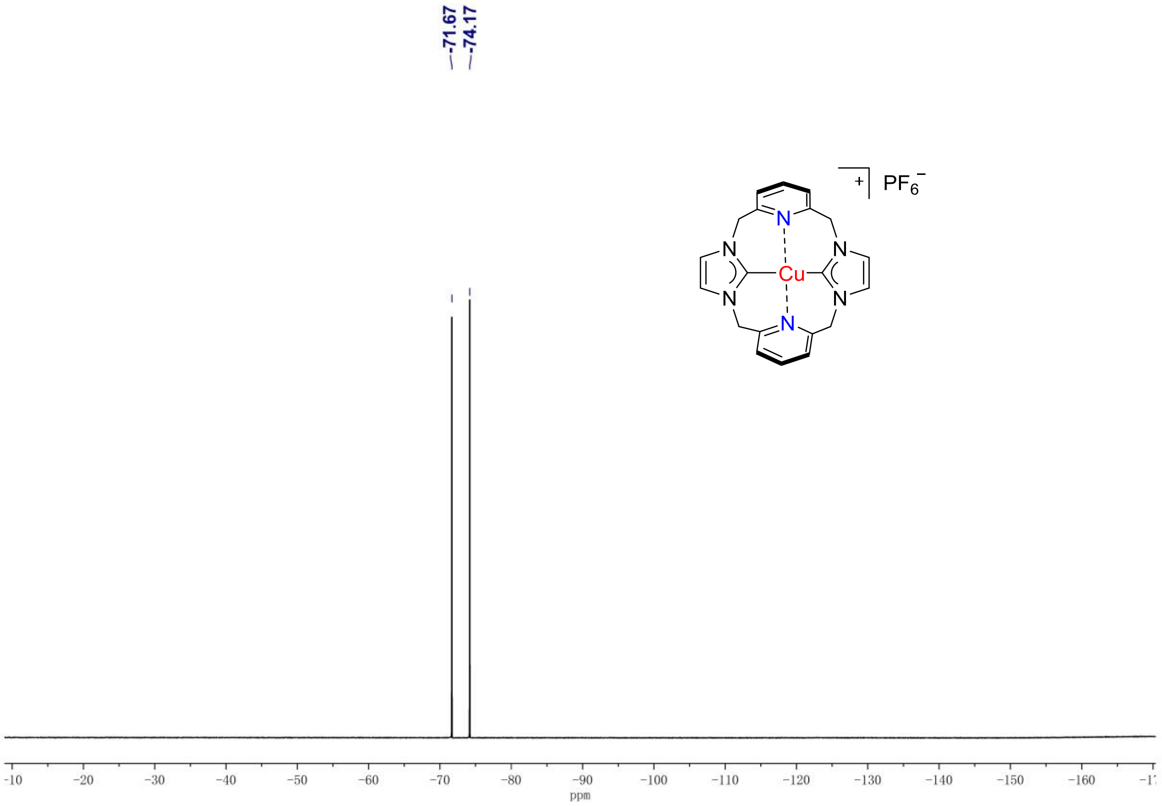

Figure S18. ^{19}F NMR spectrum of [LCu](PF_6) (**1**) in [D_3]MeCN (283 MHz, 298 K).

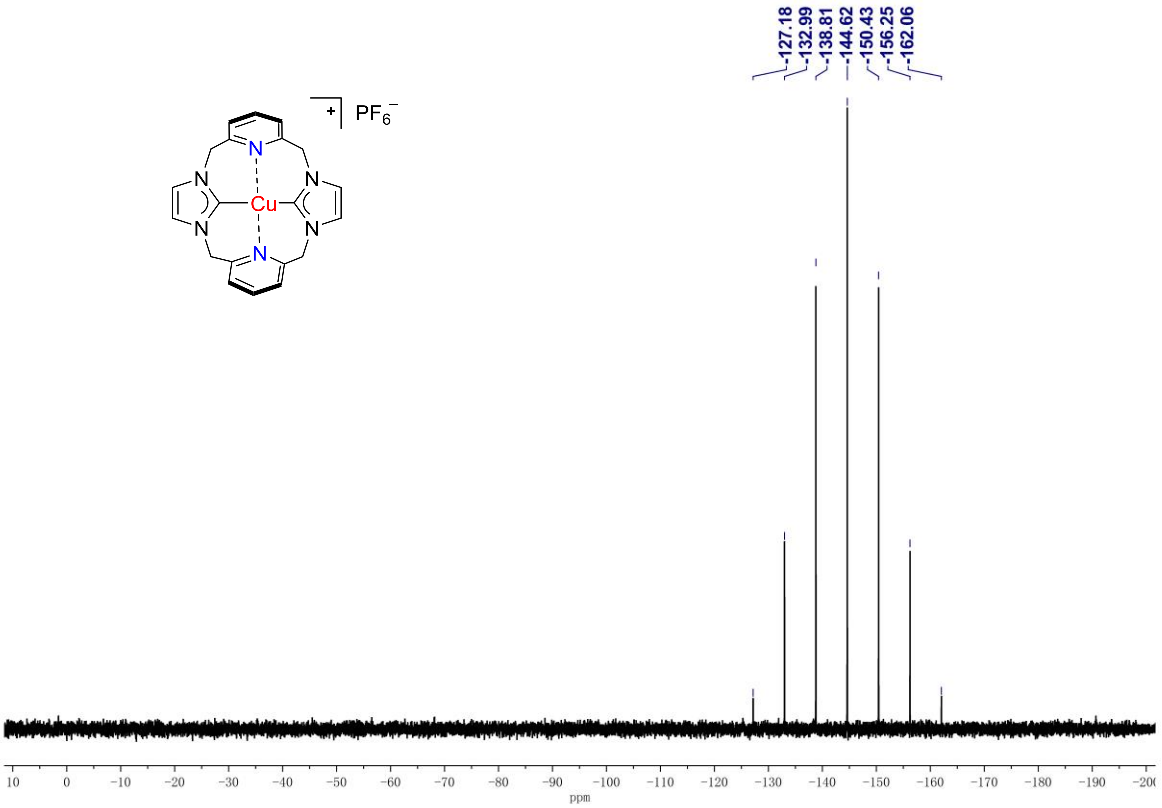

Figure S19. ^{31}P NMR spectrum of [LCu](PF_6) (**1**) in [D_3]MeCN (122 MHz, 298 K)

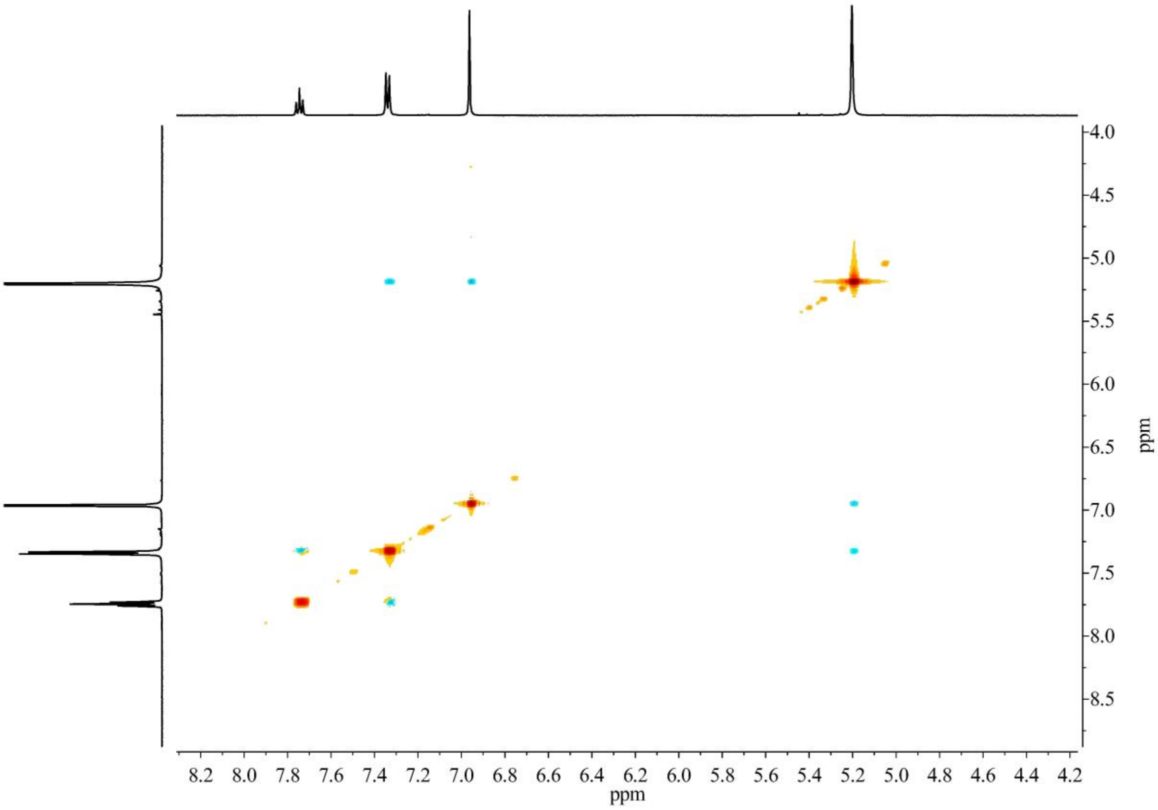

Figure S20. ^{1}H-^{1}H NOESY spectrum of [LCu](PF$_6$) (**1**) in [D$_3$]MeCN (500, 500 MHz, 298 K).

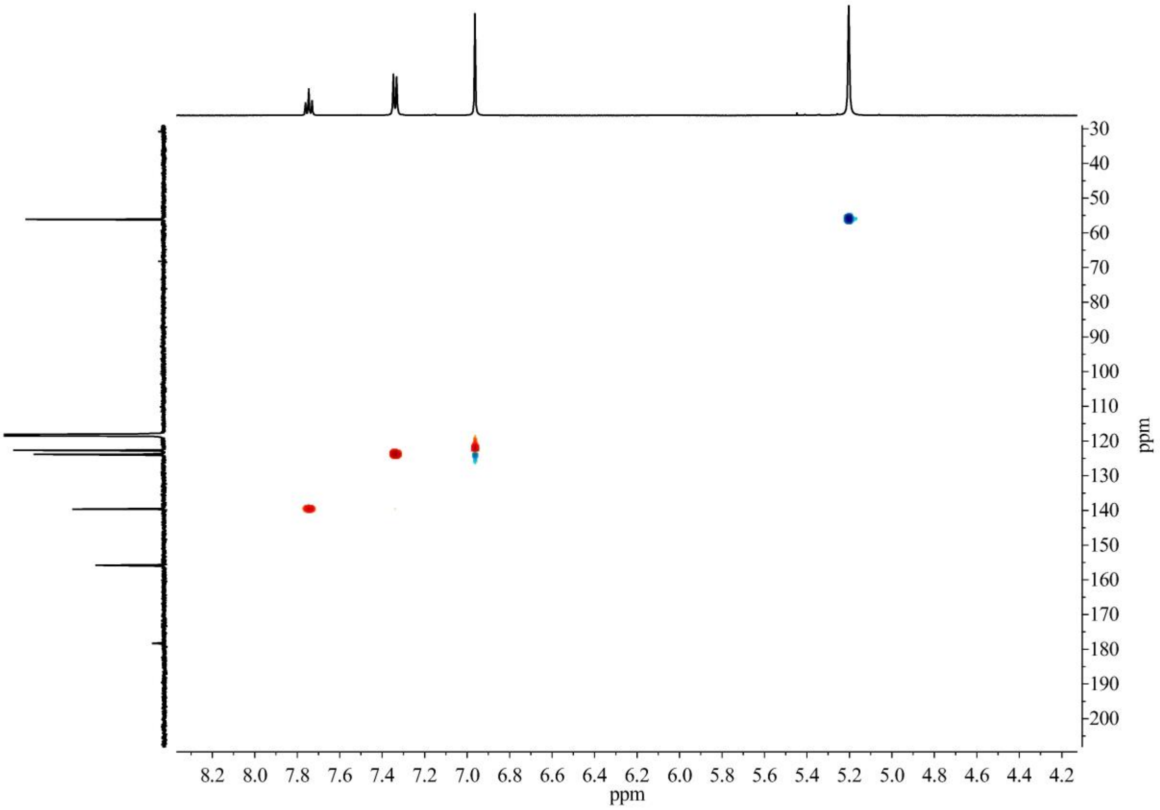

Figure S21. ^{1}H-^{1}C HSQC spectrum of [LCu](PF$_6$) (**1**) in [D$_3$]MeCN (500, 125 MHz, 298 K).

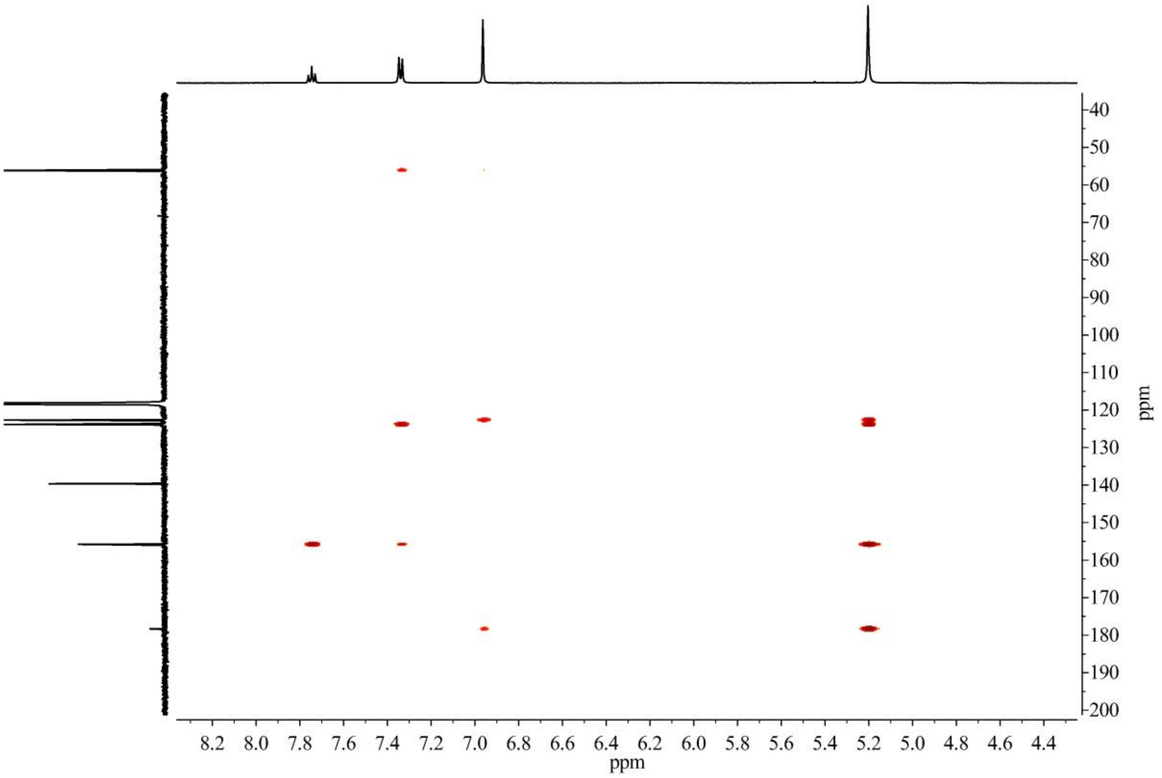

Figure S22. ^{1}H-^{1}C HMBC spectrum of [LCu](PF$_6$) (**1**) in [D$_3$]MeCN (500, 125 MHz, 298 K).

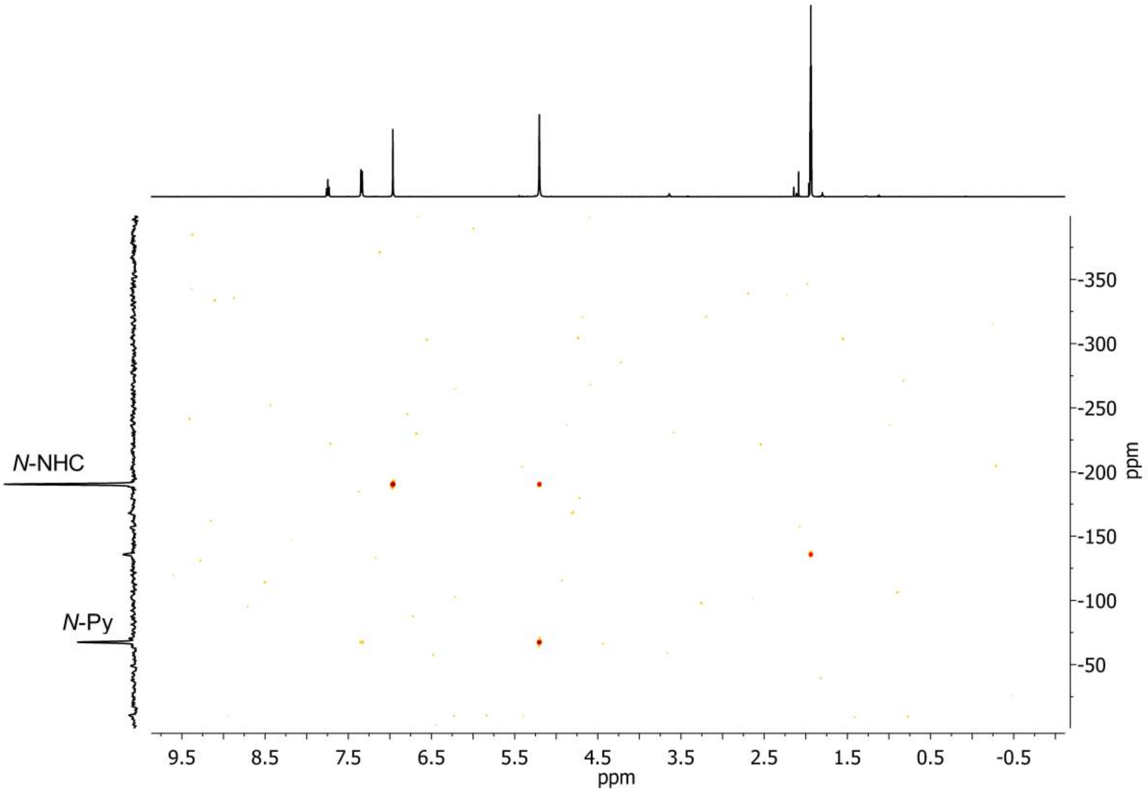

Figure S23. ^{1}H-^{15}N HMBC spectrum of [LCu](PF$_6$) (**1**) in [D$_3$]MeCN (500, 50 MHz, 298 K).

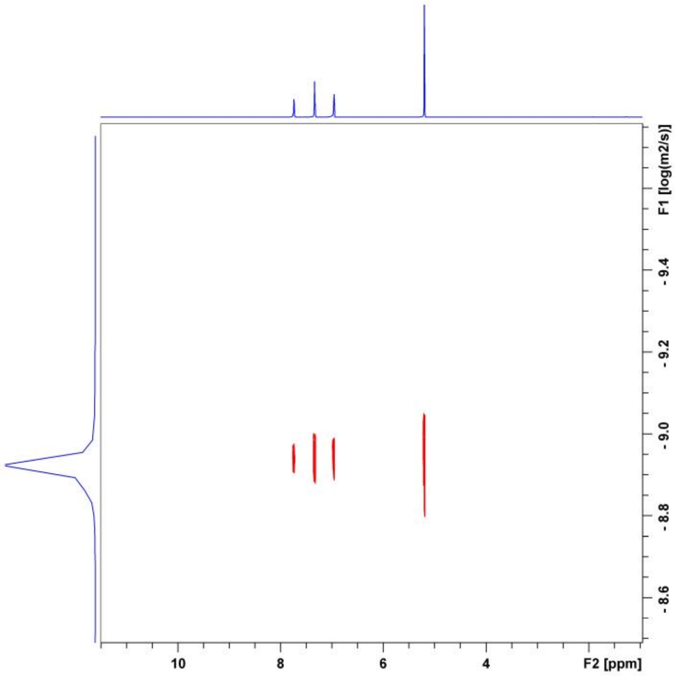

Figure S24. DOSY spectrum of [LCu](PF_6) (**1**) in [D_3]MeCN (500 MHz, 298 K) with the diffusion constant on the vertical axis.

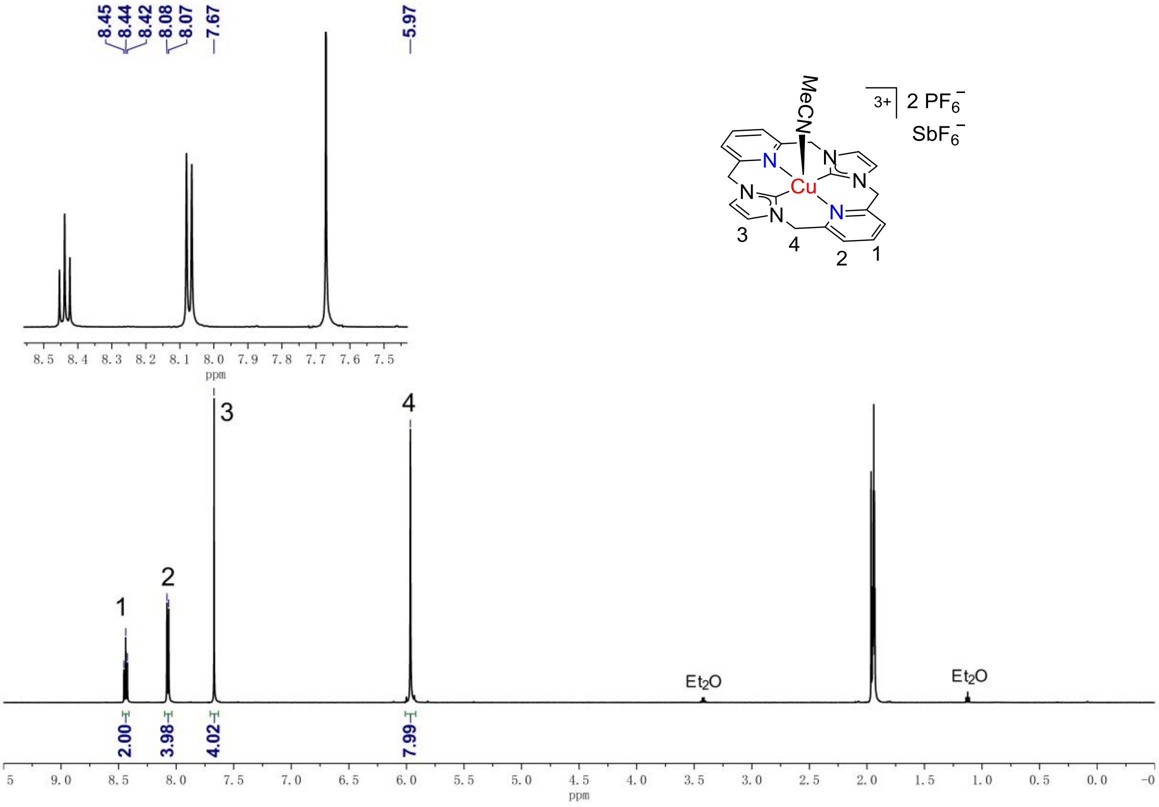

Figure S25. ^{1}H NMR spectrum of [LCu](PF_6)$_2$(SbF_6) (**3**) in [D_3]MeCN (500 MHz, 298 K).

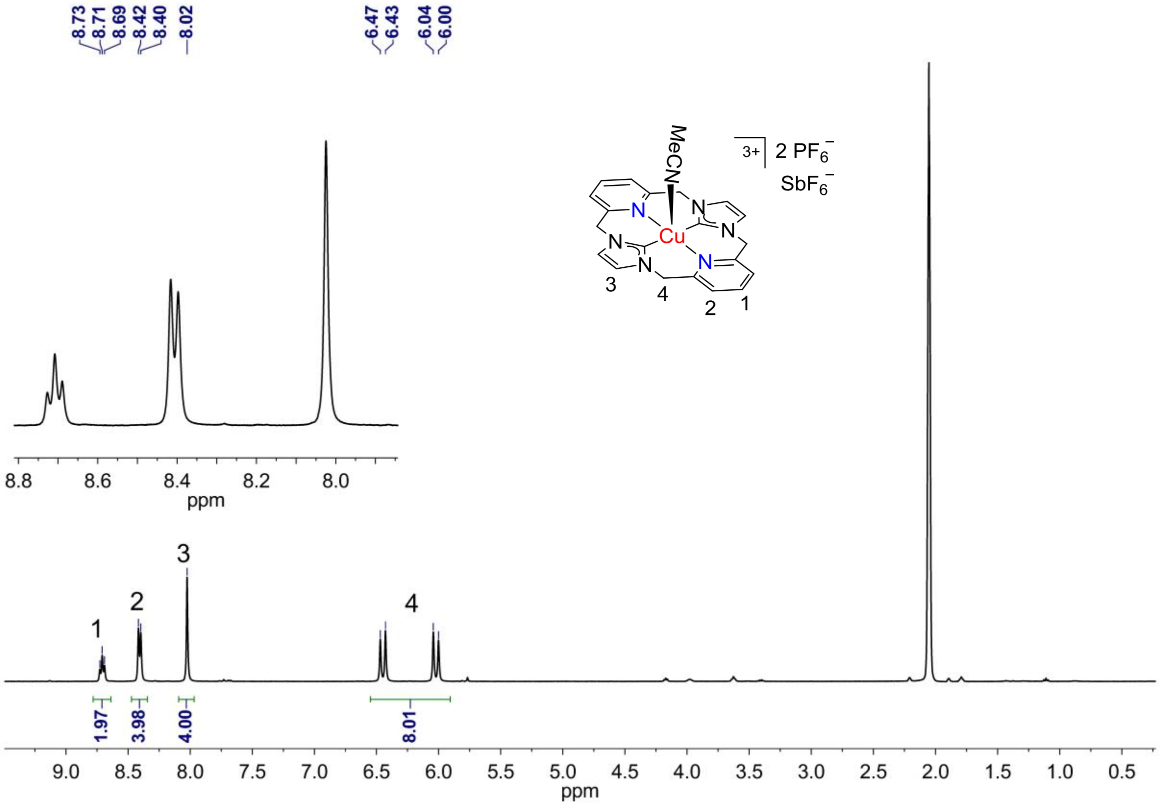

Figure S26. ^{1}H NMR spectrum of [LCu](PF$_6$)$_2$(SbF$_6$) (**3**) in [D$_6$]acetone (400 MHz, 298 K).

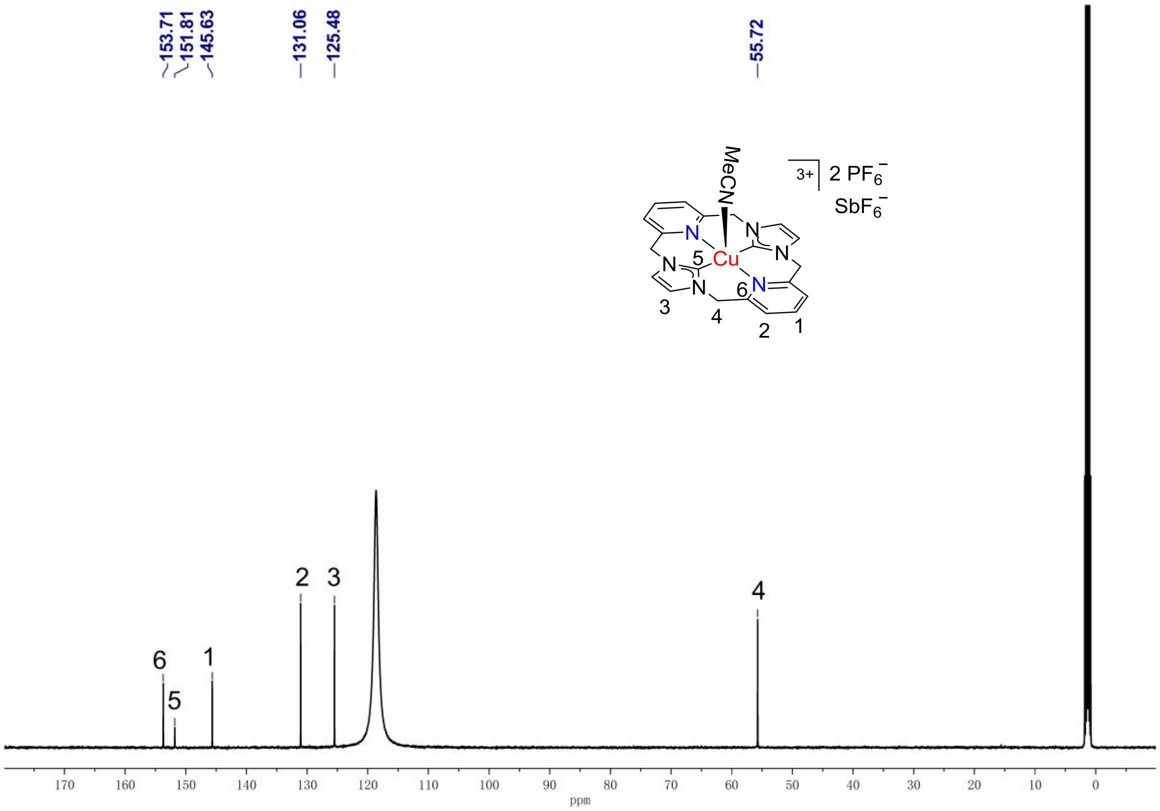

Figure S27. ^{13}C NMR spectrum of [LCu](PF$_6$)$_2$(SbF$_6$) (**3**) in [D$_3$]MeCN (125 MHz, 298 K).

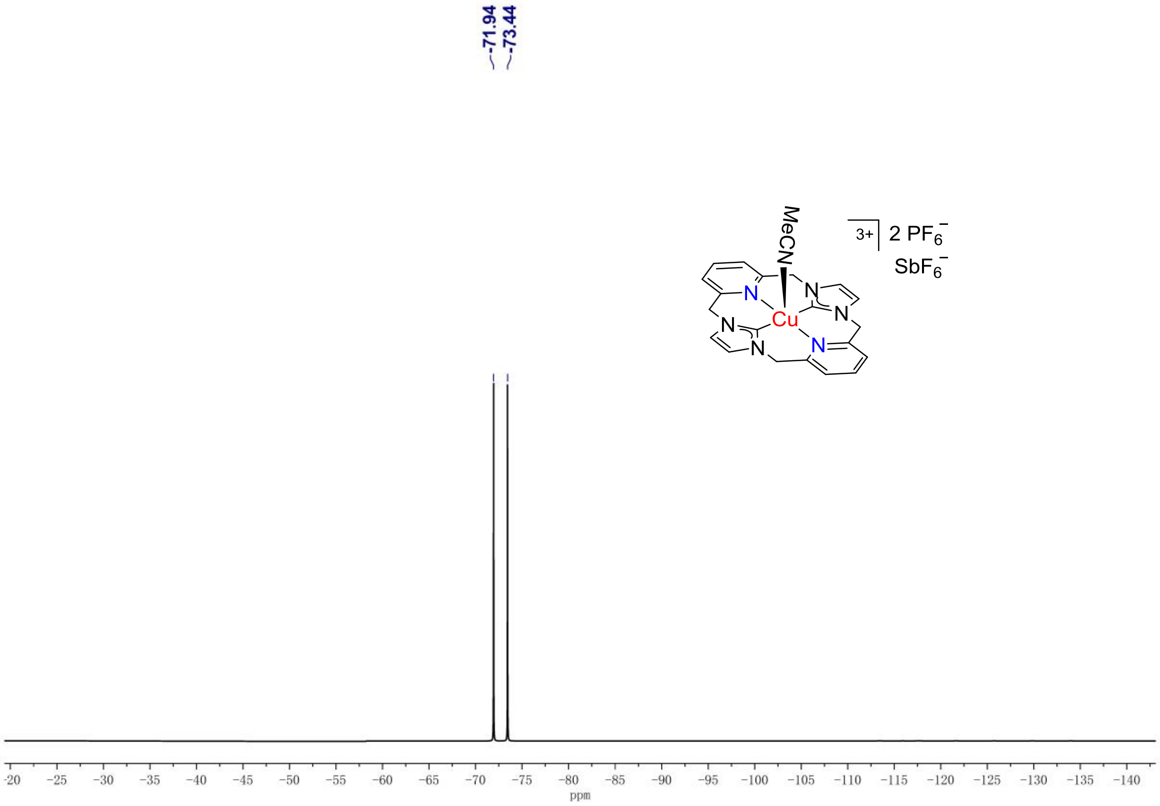

Figure S28. ^{19}F NMR spectrum of [LCu](PF$_6$)$_2$(SbF$_6$) (**3**) in [D$_3$]MeCN (471 MHz, 298 K).

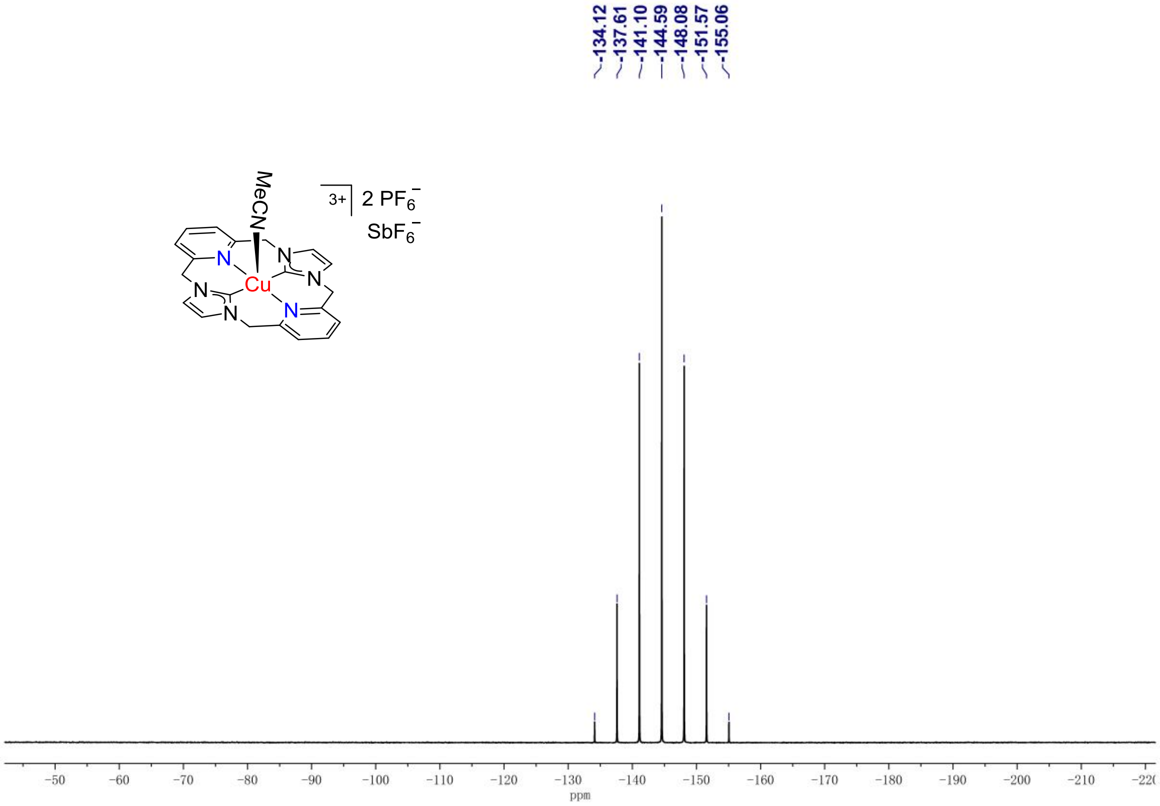

Figure S29. ^{31}P NMR spectrum of [LCu](PF$_6$)$_2$(SbF$_6$) (**3**) in [D$_3$]MeCN (203 MHz, 298 K).

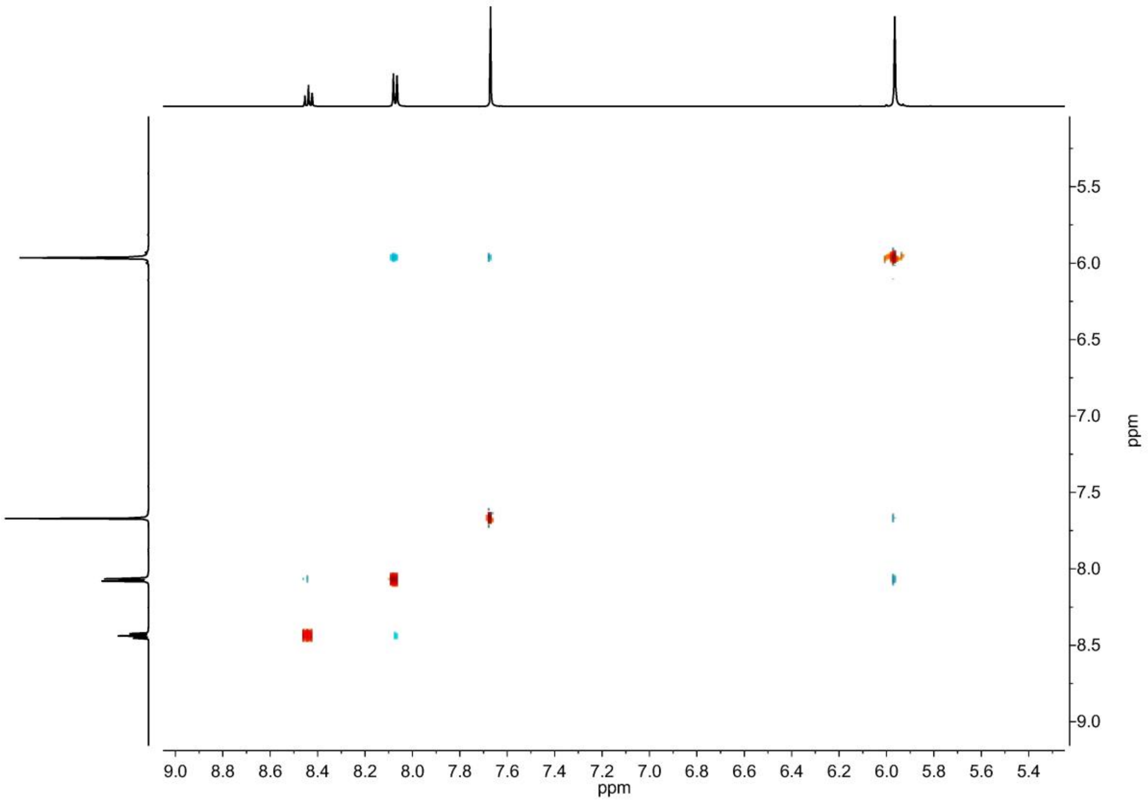

Figure S30. ^{1}H-^{1}H NOESY spectrum of [LCu](PF$_6$)$_2$(SbF$_6$) (**3**) in [D$_3$]MeCN (500, 500 MHz, 298 K).

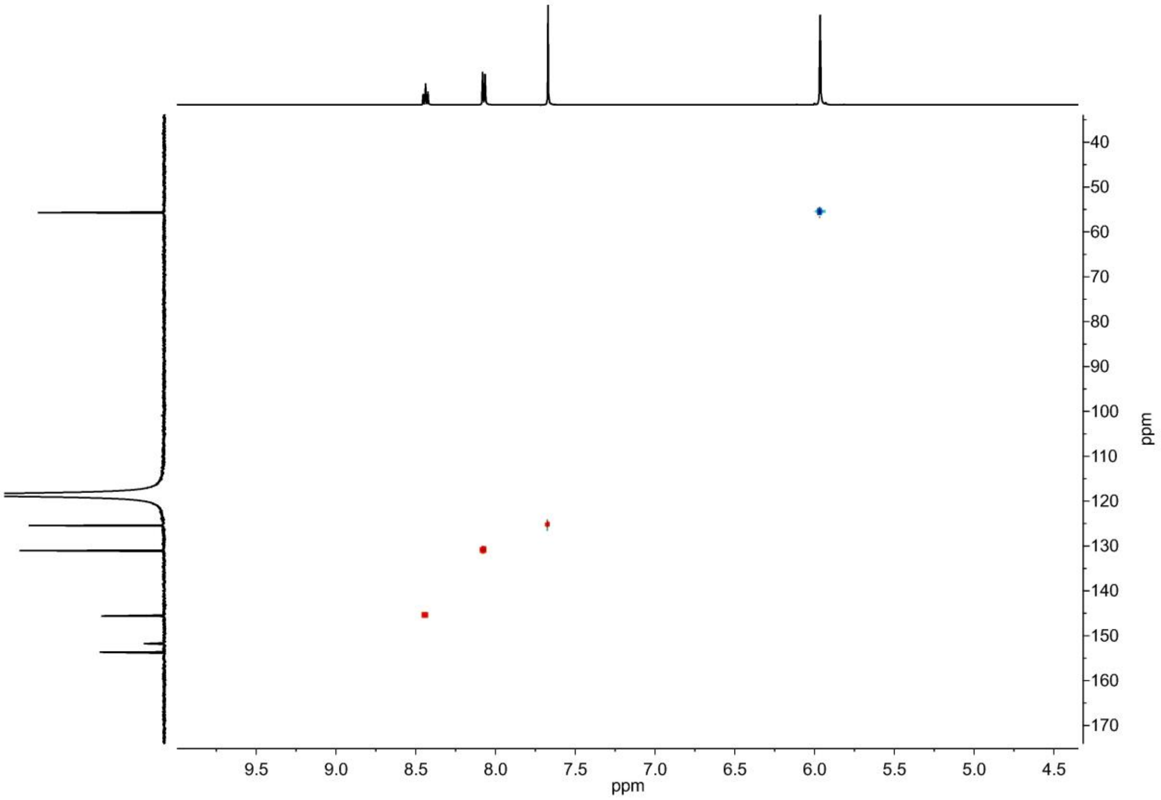

Figure S31. ^{1}H-^{13}C HSQC spectrum of [LCu](PF$_6$)$_2$(SbF$_6$) (**3**) in [D$_3$]MeCN (500, 125 MHz, 298 K).

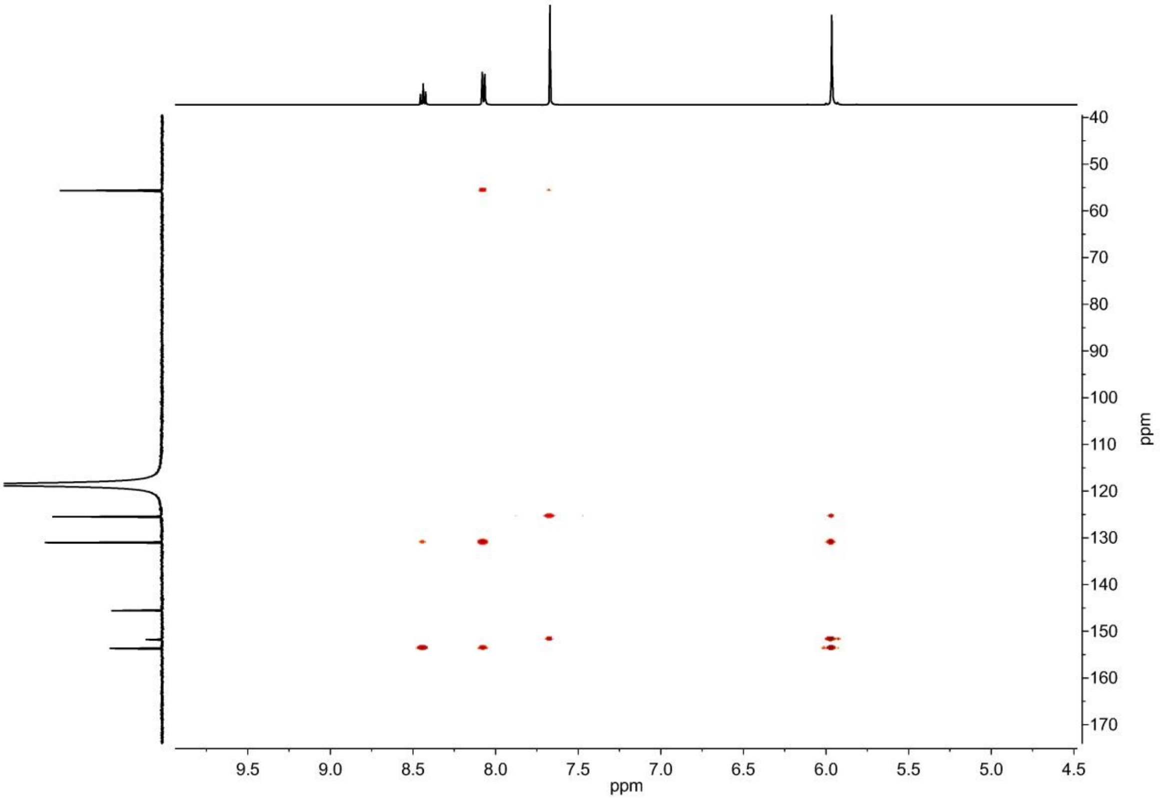

Figure S32. ^{1}H-^{13}C HMBC spectrum of $[LCu](PF_6)_2(SbF_6)$ (**3**) in $[D_3]MeCN$ (500, 125 MHz, 298 K).

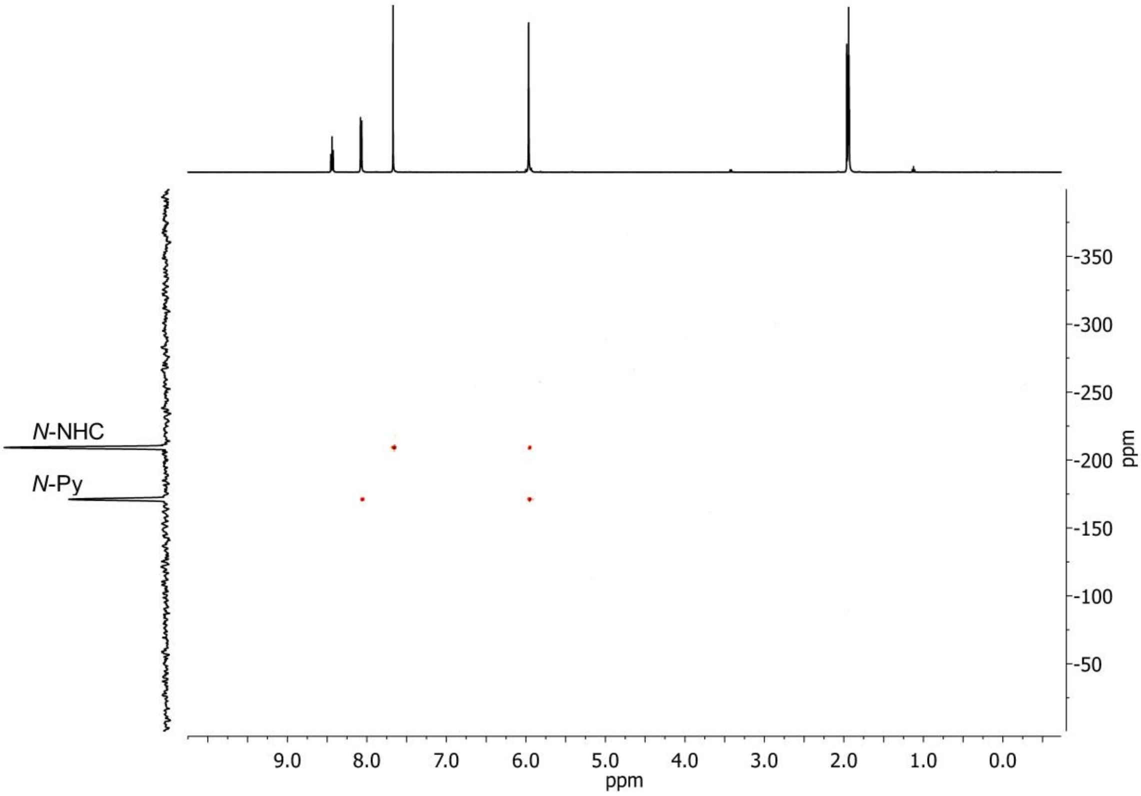

Figure S33. ^{1}H-^{15}N HMBC spectrum of $[LCu](PF_6)_2(SbF_6)$ (**3**) in $[D_3]MeCN$ (500, 50 MHz, 298 K).

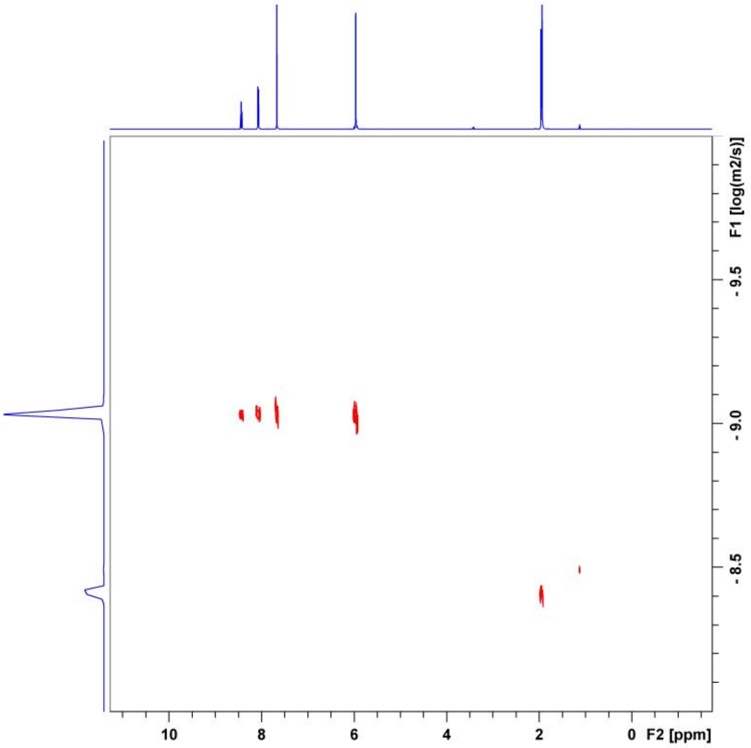

Figure S34. DOSY spectrum of [LCu]$(PF_6)_2(SbF_6)$ (**3**) in [D_3]MeCN (500 MHz, 298 K) with the diffusion constant on the vertical axis.

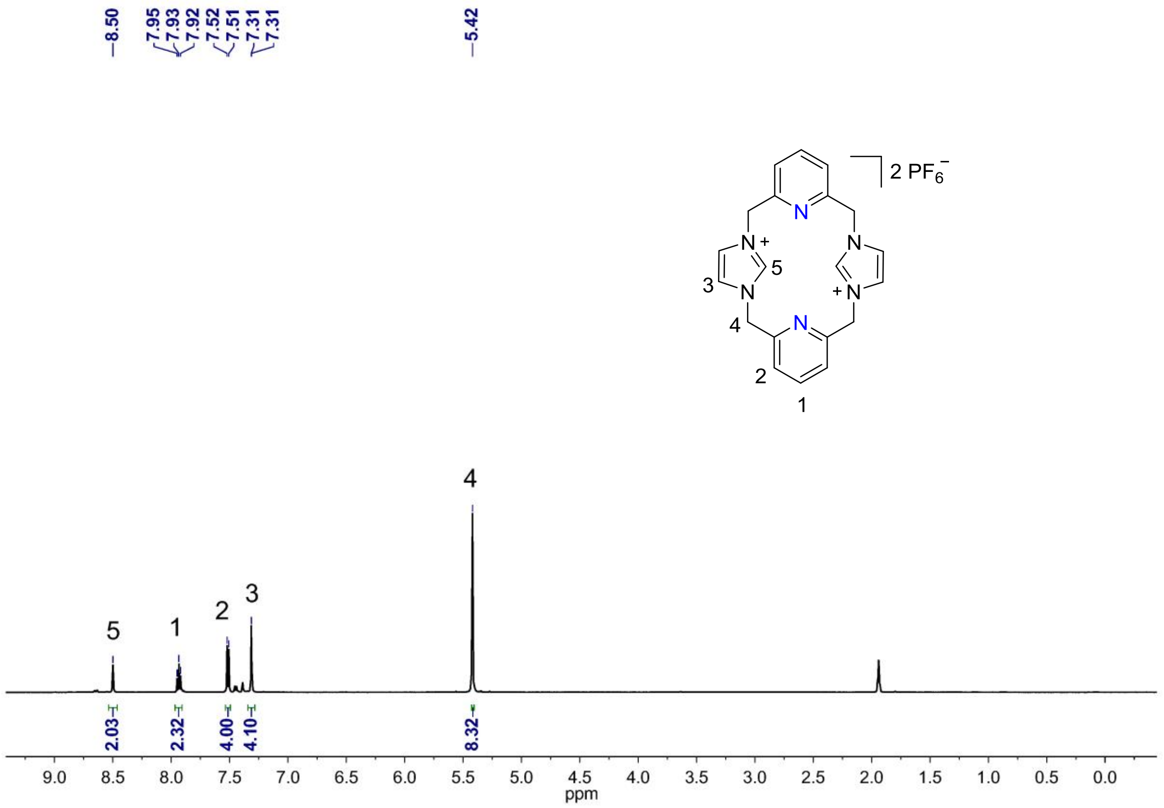

Figure S35. ^{1}H NMR spectrum of [H_2L]$(PF_6)_2$ in [D_3]MeCN (500 MHz, 298 K).

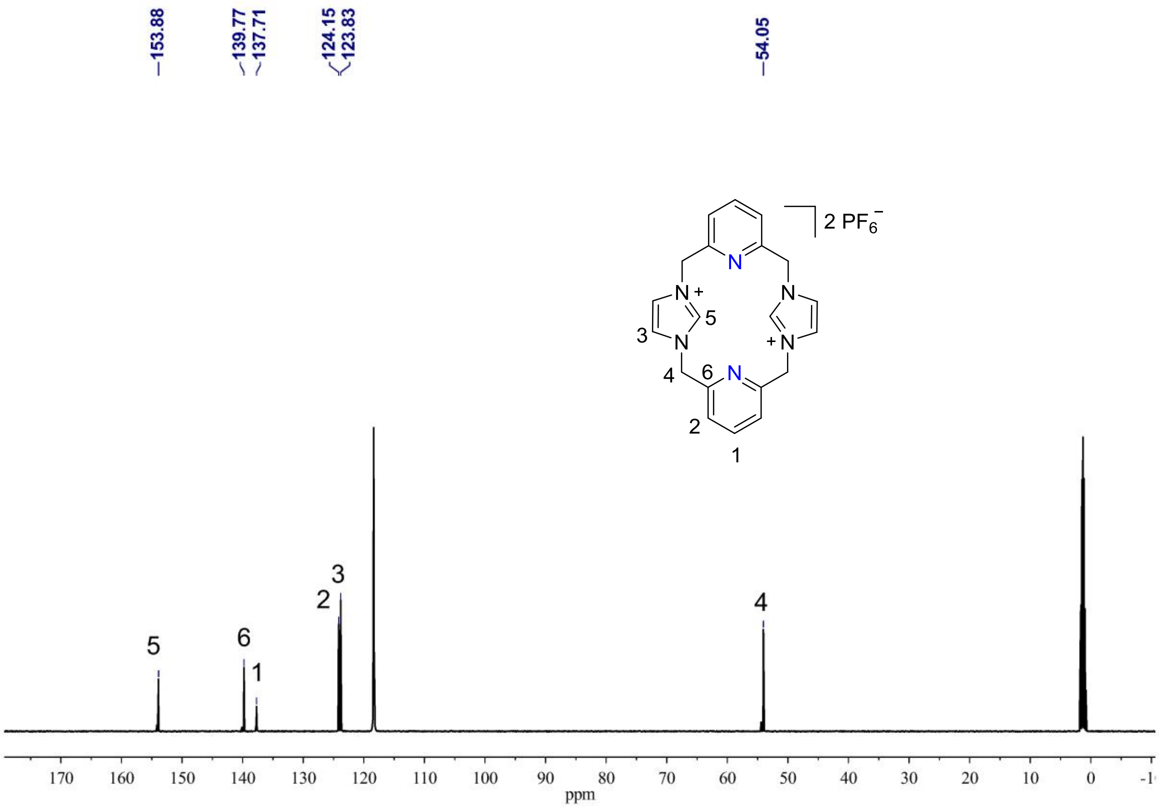

Figure S36. ^{13}C NMR spectrum of $[H_2L](PF_6)_2$ in $[D_3]MeCN$ (125 MHz, 298 K).

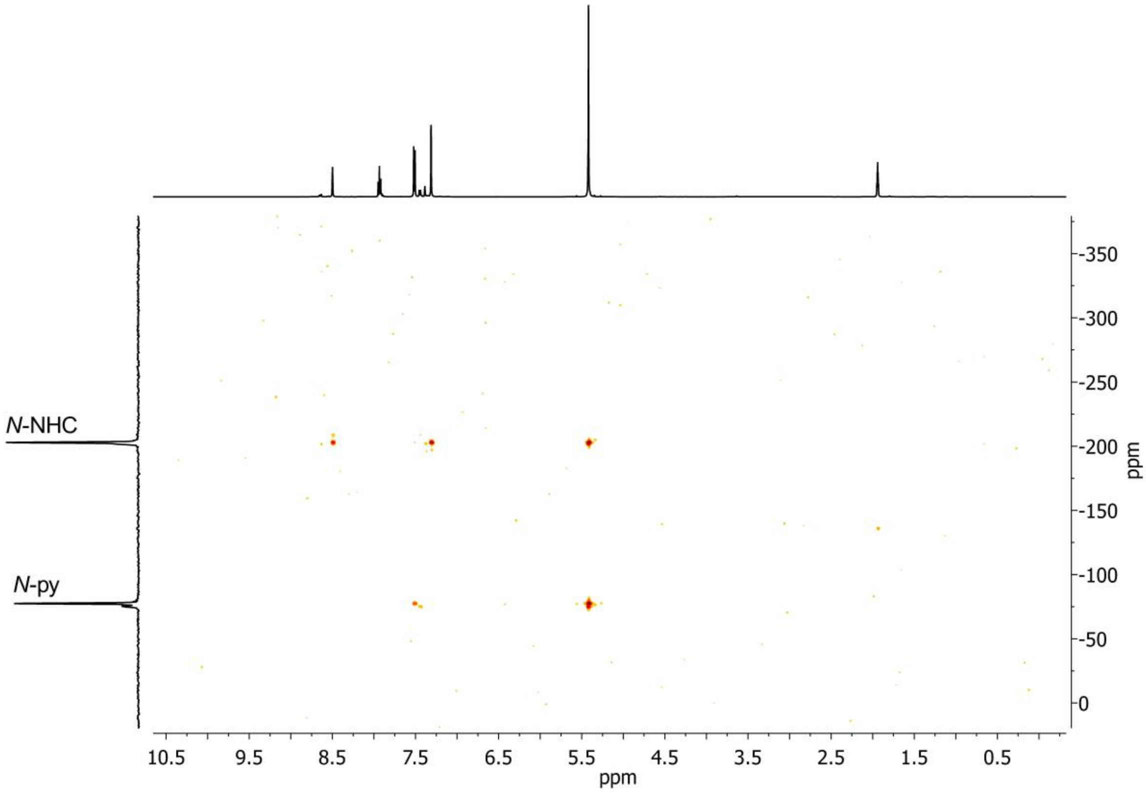

Figure S37. ^{1}H-^{15}N HMBC spectrum of $[H_2L](PF_6)_2$ in $[D_3]MeCN$ (500, 50 MHz, 298 K).

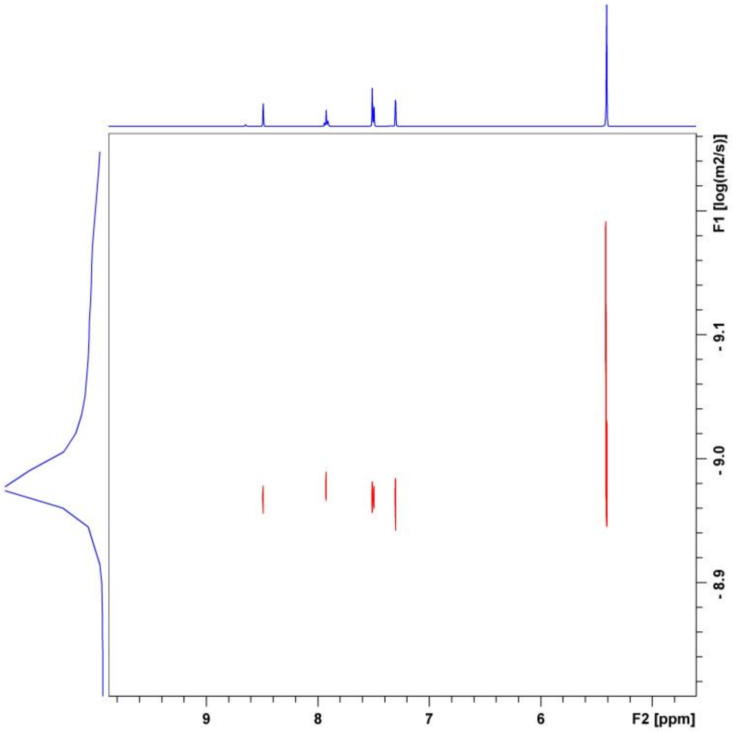

Figure S38. DOSY spectrum of $[H_2L](PF_6)_2$ in $[D_3]MeCN$ (500 MHz, 298 K) with the diffusion constant on the vertical axis.

10. Variable-Temperature NMR Spectra

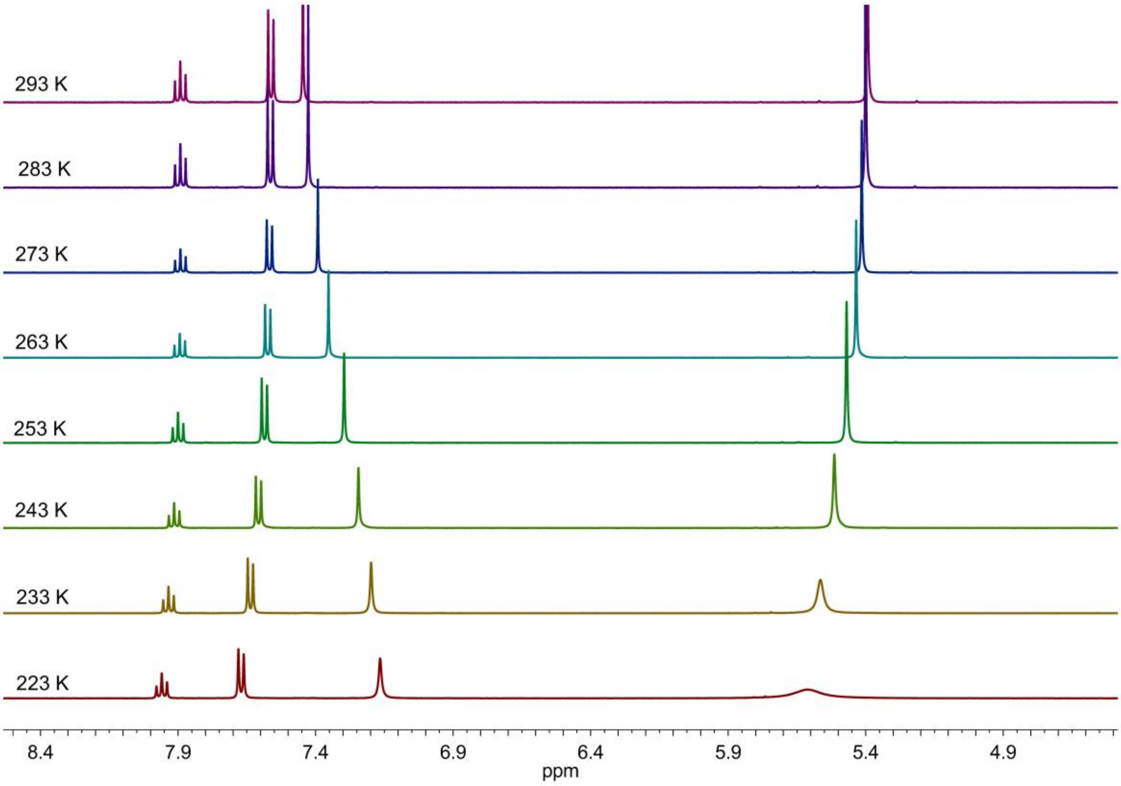

Figure S39. Variable-temperature ^{1}H NMR spectra (4.5–8.5 ppm) of [LCu](PF$_6$) (**1**) in [D$_6$]acetone (400 MHz, temperature range from 293 K to 223 K). The shifts of these peaks are visible.

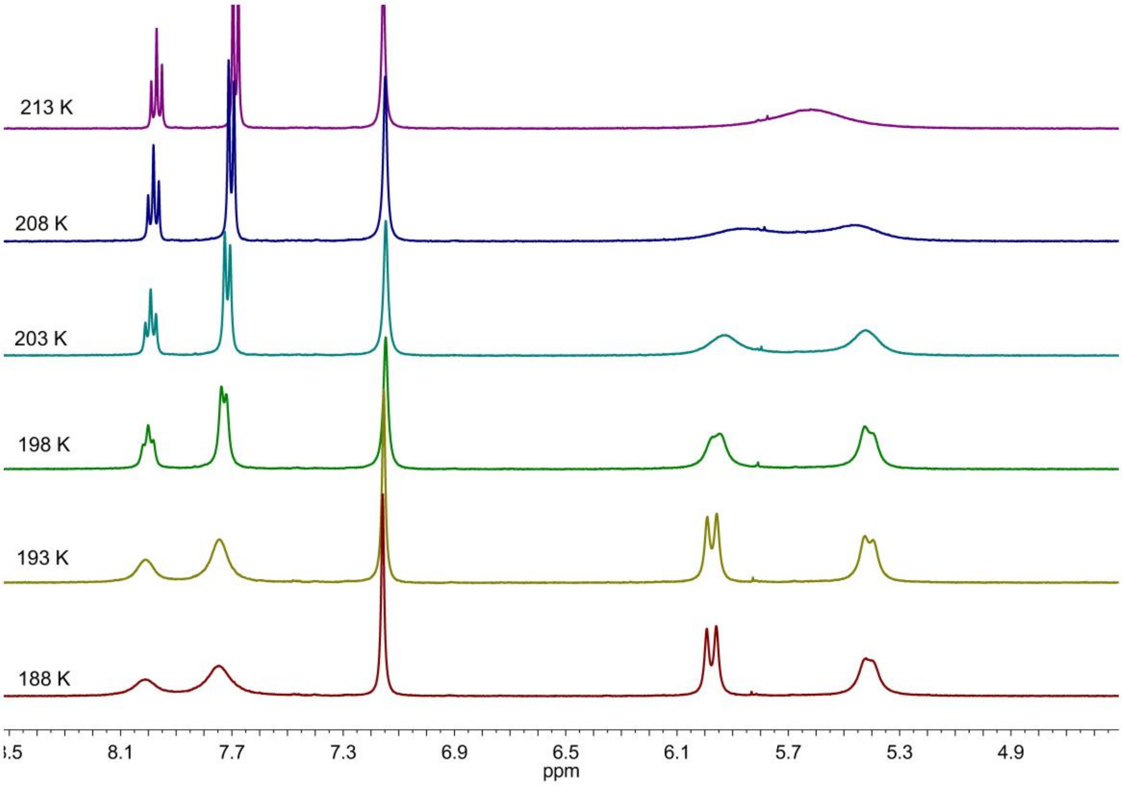

Figure S40. Variable-temperature ^{1}H NMR spectra (4.5–8.5 ppm) of [LCu](PF$_6$) (**1**) in [D$_6$]acetone (400 MHz, temperature range from 213 K to 188 K). The dynamic behavior of CH_2-linkers is visible.

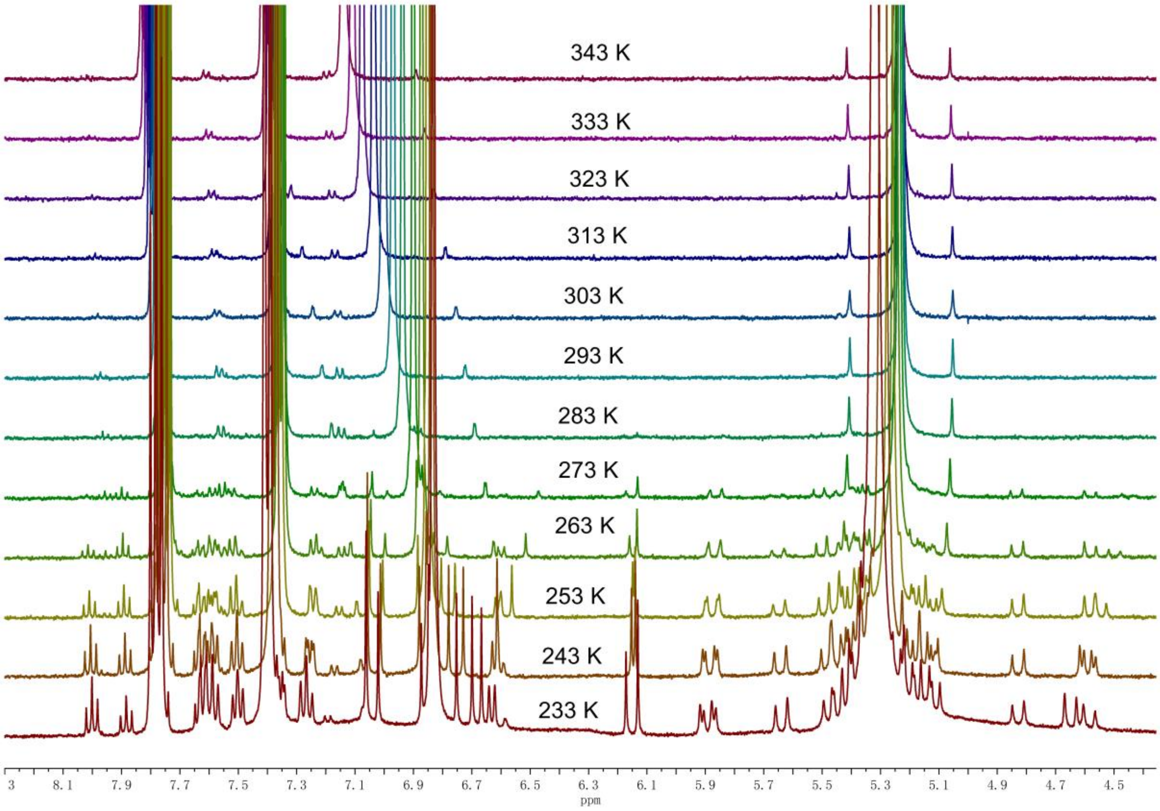

Figure S41. Variable-temperature ^{1}H NMR spectra (4.3–8.3 ppm) of [LCu](PF$_6$) (**1**) in [D$_3$]MeCN (400 MHz, temperature range from 343 K to 233 K).

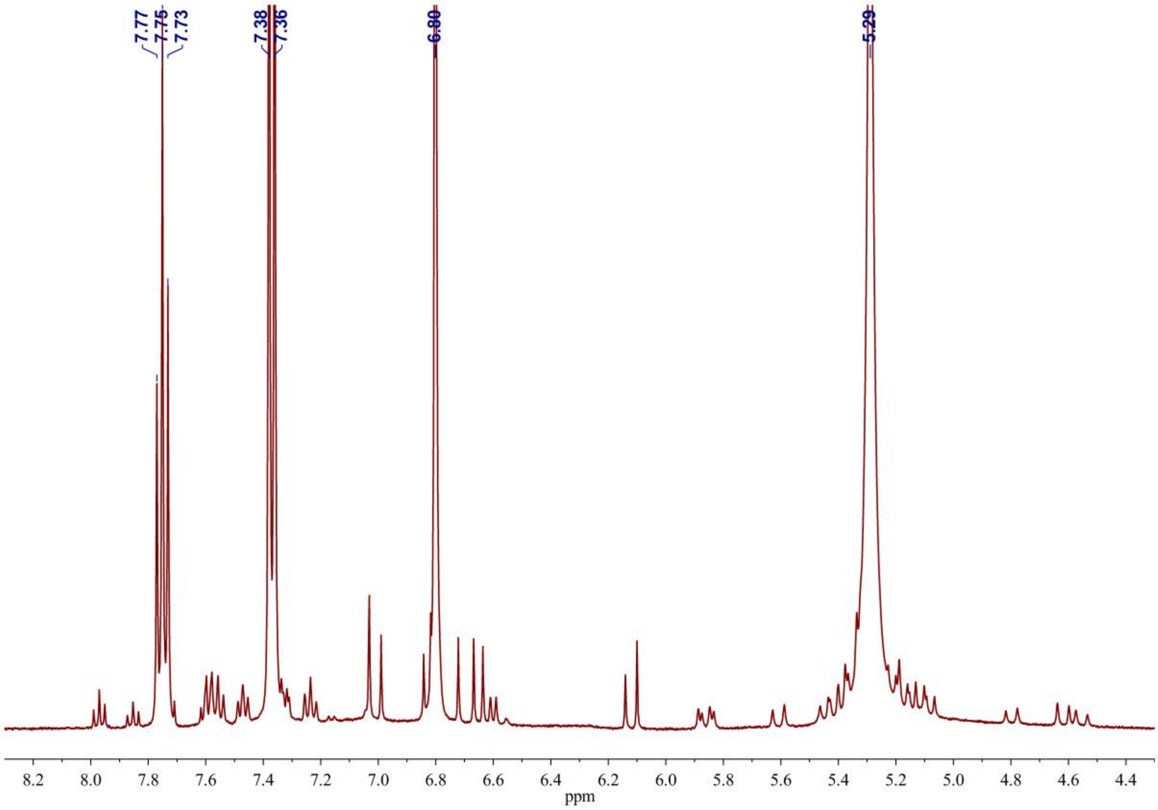

Figure S42. ^{1}H NMR spectrum (4.3–8.3 ppm) of [LCu](PF$_6$) (**1**) in [D$_3$]MeCN at 233 K (400 MHz).

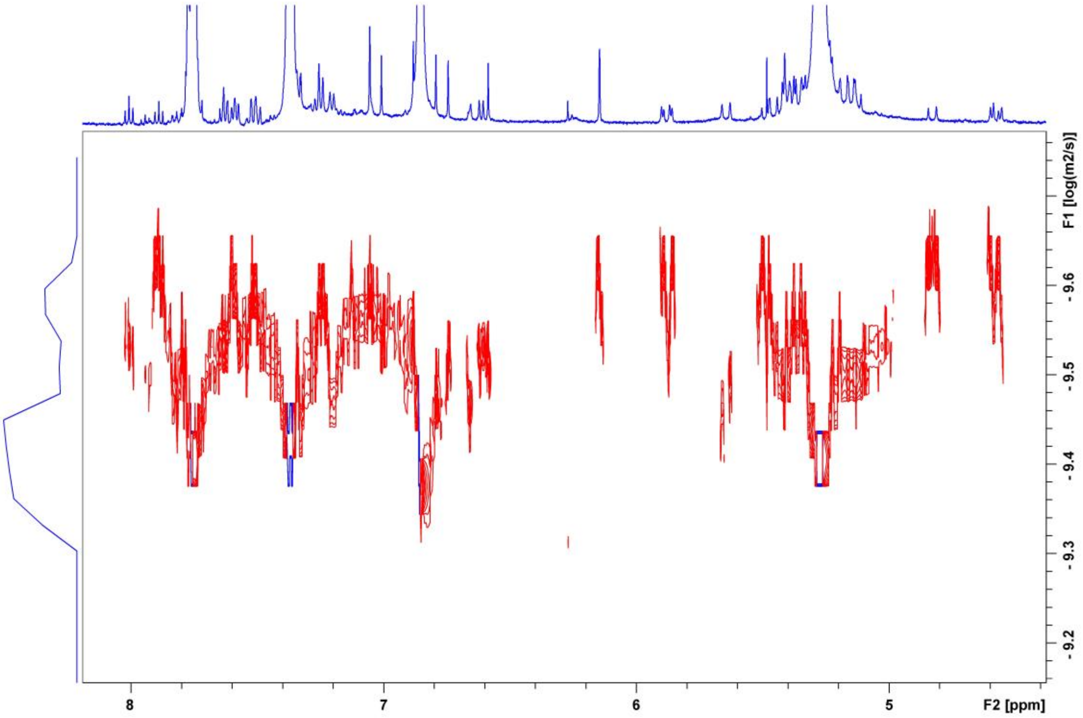

Figure S43. DOSY spectrum (4.3–8.3 ppm) of [LCu](PF$_6$) (**1**) in [D$_3$]MeCN (500 MHz, 233 K) with the diffusion constant on the vertical axis.

To determine thermodynamic parameters for the ring flip of **1**, the rate constants were calculated according to the formulas in literature.[15] The line width at half height was determined by using the line fitting function of MestReNova program. Ring flip was assumed to be frozen at 188 K in this case. The Gibbs free energy of activation Δ‡G at coalescence temperature T_c can be calculated from equation (1). The calculations of thermodynamic parameters (activation energy, enthalpy and entropy) were done according to Arrhenius equation (2) and Eyring equation (3).

$$\Delta G^{\ddagger} = RT_c\left(In\frac{T_c}{k_c} + In\frac{k_B}{h}\right) \qquad (1)$$

$$In\,k = -\frac{E_a}{R}\frac{1}{T} + In(A) \qquad (2)$$

$$In\frac{k}{T} = -\frac{\Delta H^{\ddagger}}{R}\frac{1}{T} + \frac{\Delta S^{\ddagger}}{R} + In\frac{k_B}{h} \qquad (3)$$

Table S4. Calculated values for rate constants *k* at different temperatures *T*.

T (K)	*k* (s^{-1})	ln*k*	ln(*k*·T^{-1})
193	11.9	2.477	−2.786
198	36.8	3.605	−1.683
203	105.9	4.663	−0.651
208	358.3	5.881	0.544
210	513.3	6.241	0.894
213	894.4	6.796	1.435
223	6966.3	8.849	3.442
233	29991.9	10.309	4.858

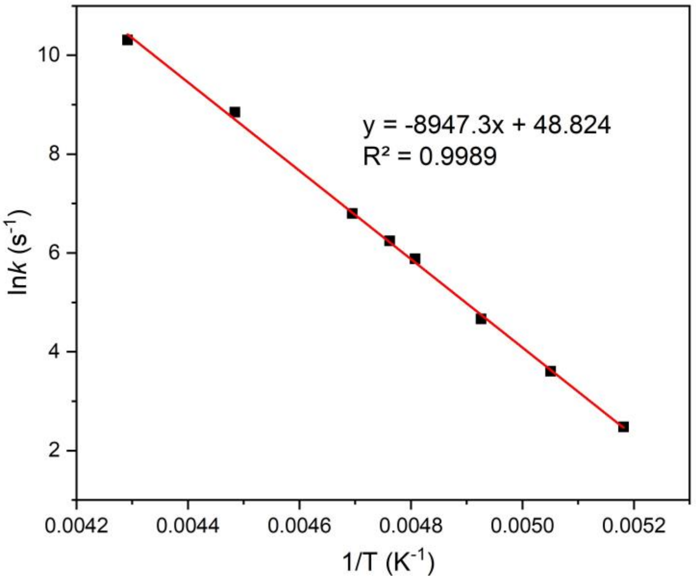

Figure S44. Arrhenius-plot for the determination of E_a of ring flip in **1**. The following value was determined: E_a = 17.8 ± 0.2 kcal/mol.

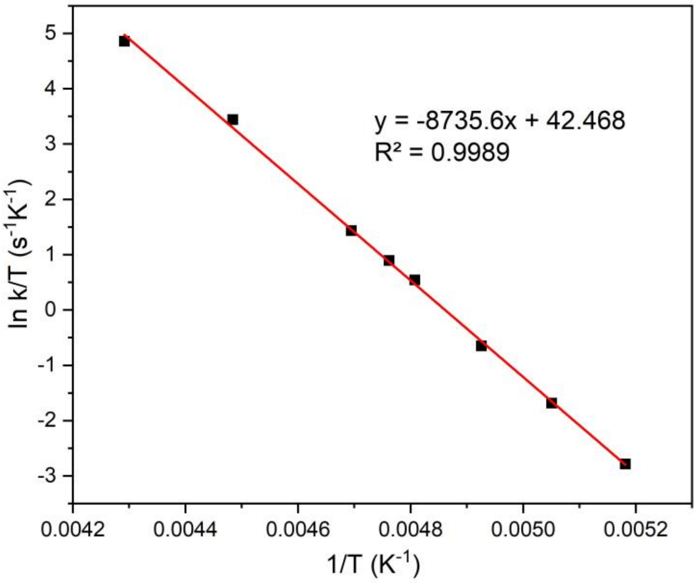

Figure S45. Eyring-plot for the determination of $\Delta H^\ddagger$ and $\Delta S^\ddagger$ of ring flip in **1**. The following values were determined: $\Delta H^\ddagger$ = 17.4 ± 0.2 kcal·mol^{-1}, $\Delta S^\ddagger$ = 37.2 ± 1.1 cal·mol^{-1}·K^{-1}.

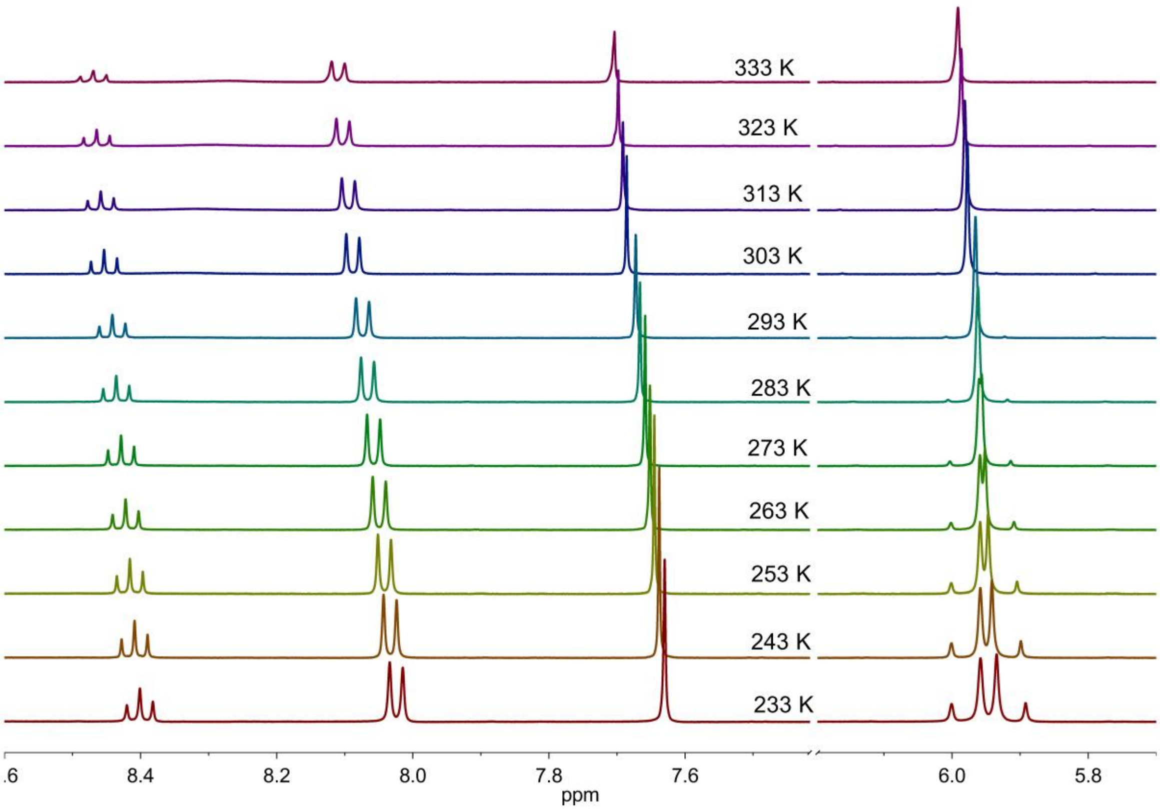

Figure S46. Variable-temperature ^{1}H NMR spectra (5.7–6.2 ppm and 7.4−8.6 ppm) of [LCu](PF$_6$)$_2$(SbF$_6$) (**3**) in [D$_3$]MeCN (400 MHz, temperature range from 333 K to 233 K).

11. DFT calculations

The ring flip was investigated based on theoretical calculations. Besides the approximately C_{2v} symmetric **1** a second stable conformer with apparent C_{2h} symmetry has been considered (Figure S47, right). The energy difference between the two conformers is negligible (< 1 kcal/mol). For the transition state, an energy difference of 8.2 kcal/mol was determined. In that case the pyridyl groups are more or less orthogonal and the apparent point group is reduced to C_S. Since the energy difference is not very high, it seems reasonable that fast ring flipping of the pyridyl groups occurs at elevated temperatures. The point group of the averaged (on the NMR time scale) molecular structure at room temperature would then be D_{2h} (i.e. all non-hydrogen atoms are in-plane), which would result in chemically equivalent methylene protons in the NMR spectra.

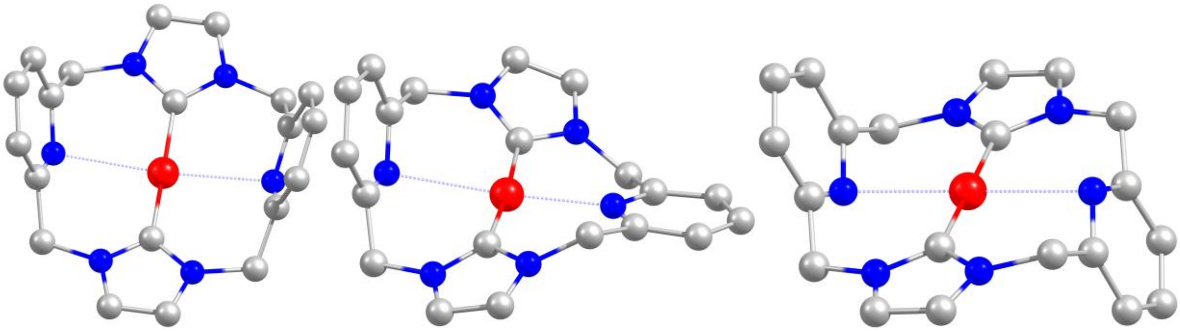

Figure S47. Calculated structures of **1**: C_{2v}, transition state (C_S), and C_{2h} conformers (from left to right). Relative energies: 0, 8.19, and 0.34 kcal/mol (from left to right). Color code: Cu = red, N = blue, C = grey.

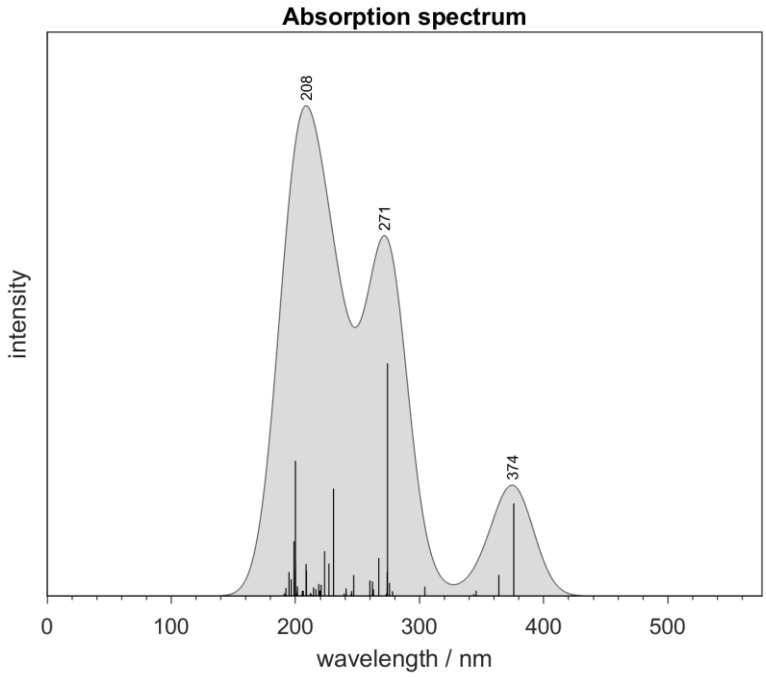

Figure S48. Calculated absorption spectra of the cation of **1**. The spectrum was convoluted using a Gaussian line shape function with a half-width of 20 nm.

Table S5. Selected TD-DFT (B3LYP/TZVP level) calculated energies, oscillator strengths, and compositions of the major electronic transitions of the cation of **1**.

States	Energy (cm^{-1})	Wavelength (nm)	Osc. Strength	Major contributions
1	26600.9	375.9	0.069980643	HOMO → LUMO (MLCT, 100%)
8	36463.7	274.2	0.175891780	H−1 → L+3 (MLCT, 82%), HOMO → L+5 (MLCT, 8%)
36	43347.9	230.7	0.081178678	H−6 → L+1 (MLCT, 62%), H−10 → L+2 (Ligand, 7%)
72	50005.0	200.0	0.102282271	HOMO → L+9 (MLCT, 71%), H−11 → L+2 (Ligand, 6%)

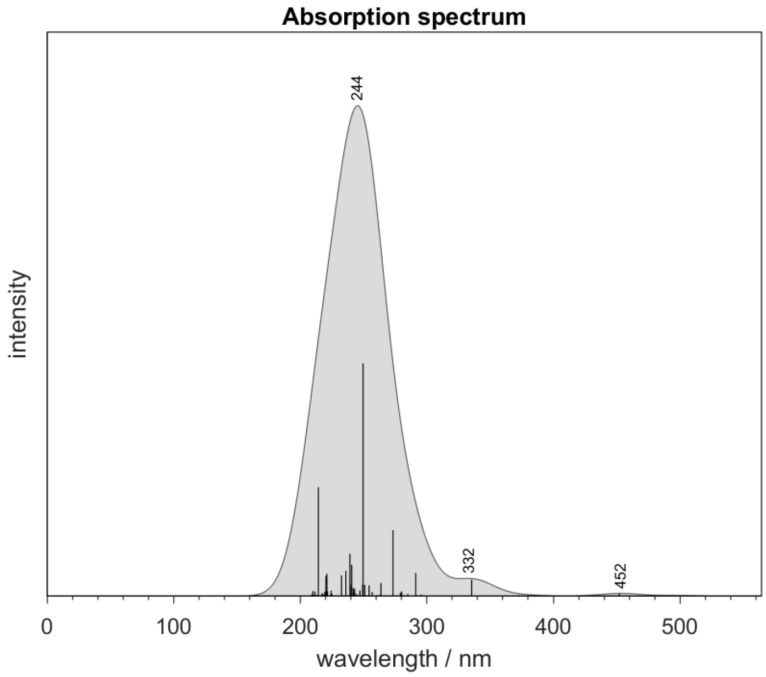

Figure S49. Calculated absorption spectra of the cation of **2**. The spectrum was convoluted using a Gaussian line shape function with a half-width of 20 nm.

Table S6. Selected TD-DFT (B3LYP/TZVP level) calculated energies, oscillator strengths, and compositions of the major electronic transitions of the cation of **2**.

States	Energy (cm^{-1})	Wavelength (nm)	Osc. Strength	Major contributions
3	22120.7	452.1	0.002741217	H−12 (b) → HOMO (d-d, 46%), H−8 (b) → HOMO (LMCT, 22%), H−6 (b) → HOMO (LMCT, 19%)
8	29816.7	335.4	0.016772805	H−1 (b) → HOMO (LMCT, 46%); H−8 (b) → HOMO (LMCT, 18%); H−6 (b) → HOMO (LMCT, 12%); H−14 (b) → HOMO (d-d, 10%)
23	36595.9	273.3	0.067341253	H−6 (b) → HOMO (LMCT, 41%); H−14 (b) → HOMO (d-d, 15%); H−12 (b) → HOMO (d-d, 10%)
36	40069.0	249.6	0.237903151	H−11 (b) → HOMO (LMCT, 56%); H−12 (b) → HOMO (d-d, 11%); H−8 (b) → HOMO (LMCT, 10%)
72	46668.6	214.3	0.111235250	H−1 (a) → L+4 (a) (Ligand, 44%); H−1 (b) → L+4 (b) (Ligand, 36%)

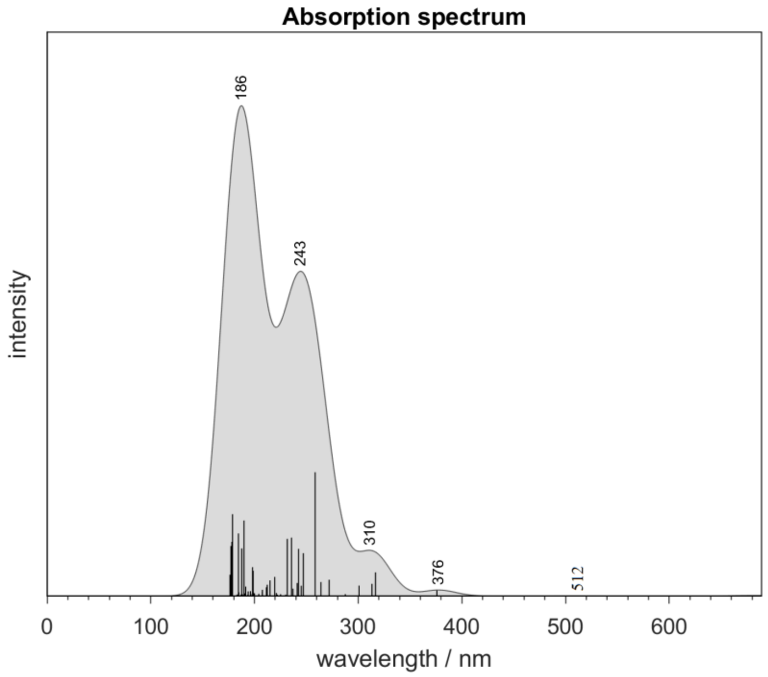

Figure S50. Calculated absorption spectra of the cation of **3**. The spectrum was convoluted using a Gaussian line shape function with a half-width of 20 nm.

Table S7. Selected TD-DFT (B3LYP/TZVP level) calculated energies, oscillator strengths, and compositions of the major electronic transitions of the cation of **3**.

States	Energy (cm^{-1})	Wavelength (nm)	Osc. Strength	Major contributions
3	19522.7	512.2	0.000601223	H−3 → LUMO (LMCT, 91%), H−2 → LUMO (LMCT, 9%)
7	26600.4	375.9	0.015659098	H−6 → LUMO (LMCT, 85%)
10	31579.9	316.7	0.066042503	H−8 → LUMO (LMCT, 64%), H−9 → LUMO (LMCT, 8%)
19	38682.2	258.5	0.345146572	H−11 → LUMO (LMCT, 46%), H−9 → LUMO (LMCT, 15%), H−12 → LUMO (LMCT, 11%)
20	40461.9	247.1	0.119544732	H−3 → L+1 (Ligand, 32%), H−21 → LUMO (d-d, 15%), H−20 → LUMO (d-d, 9%), H−12 → LUMO (LMCT, 7%)
22	41230.3	242.5	0.131725117	H−3 → L+1 (Ligand, 50%), H−2 → L+2 (Ligand, 20%)
24	42423.5	235.7	0.162963132	H−2 → L+2 (Ligand, 50%), H−1 → L+4 (Ligand, 23%)
29	43175.8	231.6	0.159393646	H−1 → L+4 (Ligand, 71%), H−2 → L+2 (Ligand, 12%)

Table S8. Comparison of the relative single-point energies obtained from the optimized geometries of **3** at different spin states.

States	RKS (*S* = 0)	UKS (*S* = 0)	UKS (*S* = 1)	BS(1,1)
E_{rel} (kcal·mol^{-1})	0	0	+25.16	+26.62

Broken-Symmetry calculations show that the high-spin state is the ground state with a coupling constant of J = 589 cm^{-1} (according to Yamaguchi).[14] The energy gap between the broken-symmetry and high-spin states is ~1.69 kcal·mol^{-1}.

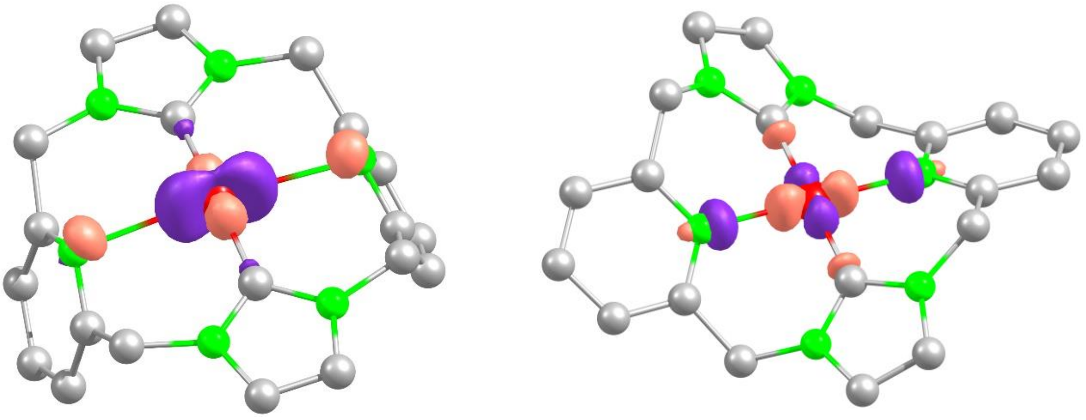

HOMO
53% Cu-3$d_{x^2-y^2}$, 4% N$^{\mathrm{Py}}$-2p (each), 4% C$^{\mathrm{NHC}}$-2p (each)

SOMO
57% Cu-3$d_{x^2-y^2}$, 6% N$^{\mathrm{Py}}$-2p (each), 5% C$^{\mathrm{NHC}}$-2p (each)

Figure S51. The HOMO of complex **1** (*S* = 0, left) and SOMO of complex **2** (*S* = 1/2, right), isodensity value = 0.08 au. The values of major orbital contributions are given. Color code: Cu = red, N = green, C = grey.

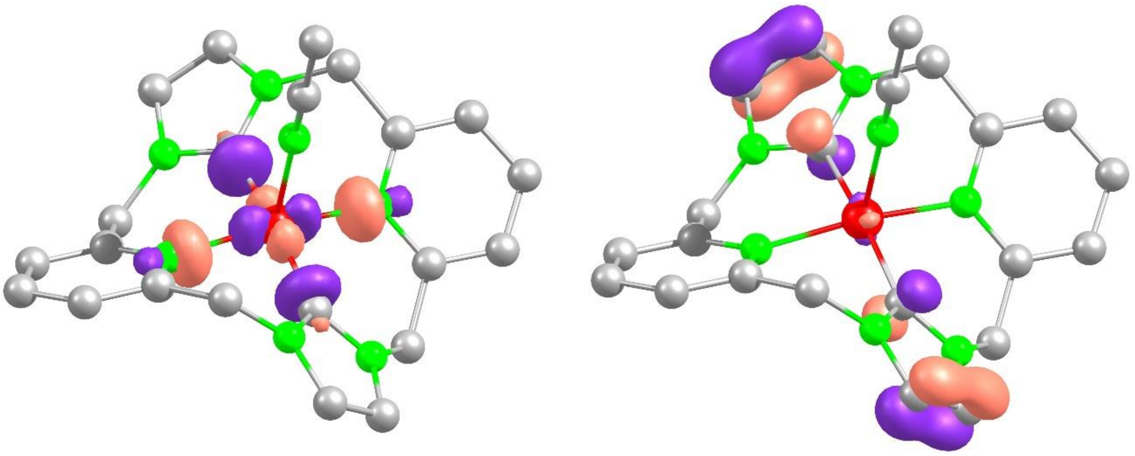

LUMO
40% Cu-3$d_{x^2-y^2}$

HOMO
3% Cu-3d_{xz}

Figure S52. The LUMO and HOMO of complex **3** (*S* = 0), isodensity value = 0.08 au. The values of *d*-orbital contribution are given. Color code: Cu = red, N = green, C = grey.

Table S9. Selected LUMOs and HOMOs of **3** in the singlet state (S = 0). Orbital energies and metal *d*-orbital contributions according to the Loewdin reduced orbital populations per MO are given.

Orbitals	Orbital energies (eV)	*d*-orbital contributions (%)
LUMO+2	−10.888	1.4 d_{yz}
LUMO+1	−11.101	0.8 d_{xy}, 1.4 d_{z^2}
LUMO	−13.378	39.5 $d_{x^2-y^2}$, 0.1 d_{z^2}
HOMO	−15.988	3.2 d_{xz}
HOMO−1	−16.040	1.0 d_{xy}, 0.6 d_{z^2}
HOMO−2	−16.611	0
HOMO−3	−16.614	0
HOMO−4	−17.379	1.5 d_{yz}
HOMO−5	−17.468	1.2 d_{yz}
HOMO−6	−17.480	2.7 d_{z^2}, 0.1 $d_{x^2-y^2}$, 0.4 d_{xy}
HOMO−7	−17.563	0.2 d_{z^2}, 0.4 $d_{x^2-y^2}$, 0.6 d_{xy}
HOMO−8	−18.035	2.5 d_{xz}, 0.1 d_{yz}
HOMO−11	−18.5126	35.4 d_{z^2}, 0.1 $d_{x^2-y^2}$, 0.2 d_{xy}

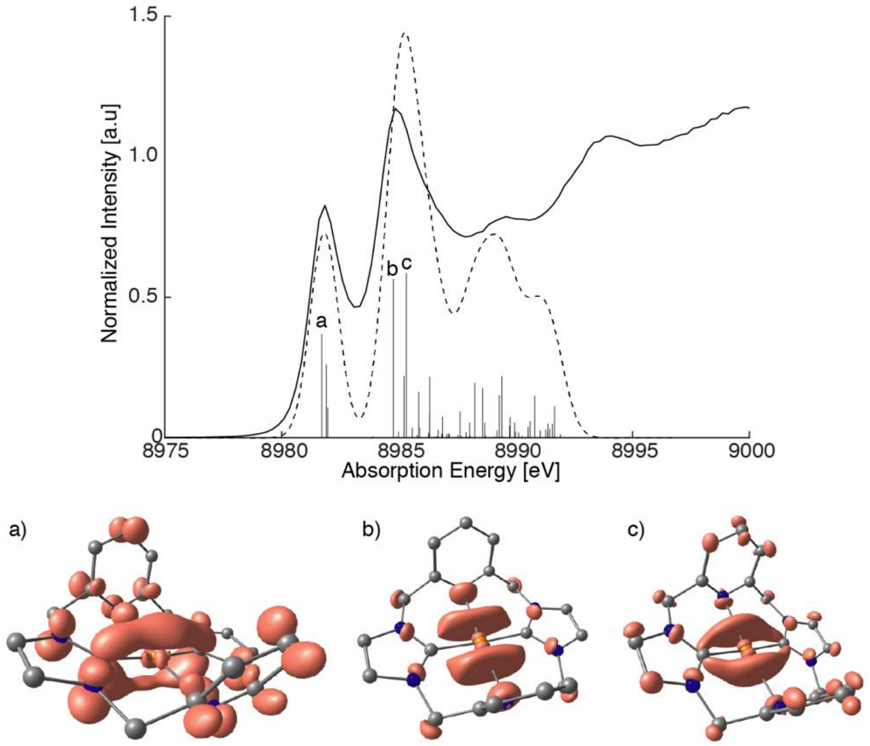

Figure S53. Cu Kβ HERFD-XAS of **1** (solid) and calculated TD-DFT spectrum (dashed) with individual transtitions (sticks). Transistion difference density plots of selected transitions are plotted below with an isosurface value of 0.002 au. The calculated spectrum is shifted by +186.7 eV. Note, this is 1.87 eV less than the shift applied to calculated spectra of **2** and **3** for the alignment of pre-edge features. Color code: C = grey, N = blue, Cu = red, hydrogens omitted.

References

[1] a) J. C. Garrison, R. S. Simons, J. M. Talley, C. Wesdemiotis, C. A. Tessier, W. J. Youngs, *Organometallics* **2001**, *20,* 1276; b) M. V. Baker, B. W. Skelton, A. H. White, C. C. Williams, *Organometallics* **2002**, *21,* 2674.

[2] a) T. Tsuda, T. Yazawa, K. Watanabe, T. Fujii, T. Saegusa, *J. Org. Chem.* **1981**, *46*, 192; b) M. Ohashi, T. Adachi, N. Ishida, K. Kikushima, S. Ogoshi, *Angew. Chem. Int. Ed.* **2017**, *56*, 11911; *Angew. Chem.* **2017**, *129,* 12073.

[3] G. J. Kubas, *Inorg. Synth.* **1990**, *28*, 68.

[4] R. Breuer, M. Schmittel, *Organometallics* **2012**, *31*, 1870.

[5] Y. Murata, F. Cheng, T. Kitagawa, K. Komatsu, *J. Am. Chem. Soc.* **2004**, *126*, 8874.

[6] E. Bill, *julX, Program for Simulation of Molecular Magnetic Data*, Max-Planck Institute for Chemical Energy Conversion, Mülheim/Ruhr, **2008**.

[7] a) G. R. Hanson, K. E. Gates, C. J. Noble, M. Griffin, A. Mitchell, S. Benson, *J. Inorg. Biochem*. **2004**, *98*, 903; b) S. Stoll, A. Schweiger, *J. Magn. Reson*. **2006**, *178*, 42.

[8] a) G. M. Sheldrick, *Acta Cryst.* **2015**, *A71*, 3; b) G. M. Sheldrick, *Acta Cryst.* **2015**, *C71*, 3.

[9] *X-RED*; STOE & CIE GmbH, Darmstadt, Germany, **2002**.

[10] P. Chandrasekaran, S. C. E. Stieber, T. J. Collins, L. Que, F. Neese, S. DeBeer, *Dalton. Trans.* **2011**, *40*, 11070.

[11] F. Neese, *WIREs Comput. Mol. Sci.* **2012**, *2*, 73.

[12] a) A. Schäfer, H. Horn, R. Ahlrichs, *J. Chem. Phys.* **1992**, *97*, 2571; b) F. Weigend, R. Ahlrichs, *Phys. Chem. Chem. Phys.* **2005**, *7*, 3297.

[13] S. Grimme, J. Antony, S. Ehrlich, S., H. Krieg, *J. Chem. Phys.* **2010**, *132*, 154104.

[14] a) K. Yamaguchi, Y. Takahara, T. Fueno in *Applied Quantum Chemistry* (Ed.: V. H. Smith), Reidel, Dordrecht, **1986**, *155*; b) T. Soda, Y. Kitagawa, T. Onishi, Y. Takano, Y. Shigeta, H. Nagao, Y. Yoshioka, K. Yamaguchi, *Chem. Phys. Lett.* **2000**, *319*, 223.

[15] a) F. P. Gasparro, N. H. Kolodny, *J. Chem. Educ.* **1977**, *54*, 258; b) J. Sandström in *Dynamic NMR Spectroscopy*, Academic Press, London, **1982**; c) P. J. Garratt, S. N. Thorn, R. Wrigglesworth, *Tetrahedron* **1994**, *50*, 12211.